TESTING AND ANALYSIS OF COMPOSITE SKIN/STRINGER DEBONDING UNDER MULTI-AXIAL LOADING

Ronald Krueger*, Michael K. Cvitkovich*, T. Kevin O'Brien**, and Pierre J. Minguet***
* National Research Council Research Associate
** U.S. Army Research Laboratory, Vehicle Technology Directorate
NASA Langley Research Center
Hampton, VA 23681
*** Boeing
Philadelphia, PA 19142

ABSTRACT

A consistent step-wise approach is presented to investigate the damage mechanism in composite bonded skin/stringer constructions under uniaxial and biaxial (in-plane/out-of-plane) loading conditions. The approach uses experiments to detect the failure mechanism, computational stress analysis to determine the location of first matrix cracking and computational fracture mechanics to investigate the potential for delamination growth. In a first step, tests were performed on specimens, which consisted of a tapered composite flange, representing a stringer or frame, bonded onto a composite skin. Tests were performed under monotonic loading conditions in tension, three-point bending, and combined tension/bending to evaluate the debonding mechanisms between the skin and the bonded stringer. For combined tension/bending testing, a unique servohydraulic load frame was used that was capable of applying both in-plane tension and out-of-plane bending loads simultaneously. Specimen edges were examined on the microscope to document the damage occurrence and to identify typical damage patterns. For all three load cases, observed failure initiated in the flange, near the flange tip, causing the flange to almost fully debond from the skin.

In a second step, a two-dimensional plane-strain finite element model was developed to analyze the different test cases using a geometrically nonlinear solution. For all three loading conditions, computed principal stresses exceeded the transverse strength of the material in those areas of the flange where the matrix cracks had developed during the tests. In a third step,

Journal of Composite Materials, Vol. 34, No. 15, 2000, pp. 1263-1300.

delaminations of various lengths were simulated in two locations where delaminations were observed during the tests. The analyses showed that at the loads corresponding to matrix ply crack initiation computed strain energy release rates exceeded the values obtained from a mixed mode failure criterion in one location. Hence, unstable delamination propagation is likely to occur as observed in the experiments.

KEY WORDS

Composite materials, testing, finite element analysis, fracture mechanics, skin/flange interface, secondary bonding.

INTRODUCTION

Carbon epoxy composite structures are widely used by today's aircraft manufacturers to reduce weight. Co-curing, co-bonding, and secondary bonding have become the most promising processes to replace traditional mechanical fastening methods. Composite materials have been introduced fairly recently into primary structures of commercial airplanes. The failure processes in composites are not as well understood as in metals. Previous investigations of the failure of secondary bonded structures were conducted with specimens cut from a full-size panel to verify the integrity of the bondline between the skin and the flange or frame [1]. However, these panels were rather expensive to produce and there was a need for a test configuration that would allow detailed observations of the failure mechanism at the skin/flange interface. Comparatively simple simulation specimens consisting of a stringer bonded onto a skin were developed and it was shown in experiments that the failure initiated at the tip of the flange, identical to the failure observed in the full-size panels and frame pull-off specimens [2-5]. Results suggested that the local force and moment resultants at the flange tip, may be used to characterize damage onset. The studies also indicated that the maximum ply principal transverse tensile stress might cause the initial failure in the form of matrix cracks from which delaminations may start to grow [2-4]. In a related study which used the same type of simulation specimen a failure criterion based on the normal strain perpendicular to the fiber direction was proposed [6].

The objective of this work was to investigate the damage mechanisms in composite bonded skin/stringer structures using a consistent step-wise approach based on experiments to detect the failure mechanism, computational stress analysis to determine the location of first matrix cracking and computational fracture mechanics to investigate the potential for delamination growth. The specimen consisted of a tapered composite flange, representing a stringer or frame, bonded onto a

composite skin. Earlier studies focussed on the influence of skin and flange layup on failure caused by three-point and four-point bending loads [2-5]. In the current invetigation, in which different load conditions were of prime interest, only one specimen configuration and layup was studied.

The first step of this work was to perform test under monotonic loading conditions in tension, three-point bending, and combined tension/bending to evaluate the debonding mechanisms between the skin and the bonded stringer. Three-point and four-point bending loading conditions as tested previously [2-5] or simple tension loading may be appropriate for a variety of applications, but in many cases composite structures may experience both bending and membrane loads during in-flight service. In the current study, therefore, the failure mechanisms under multi-axial loading were investigated, as they do not represent a simple combination of the various load components but involve interaction between the loads. For the combined multi-axial tension/bending testing, a unique servohydraulic load frame was used that was capable of applying axial tension and transverse bending loads simultaneously [7, 8]. Microscopic investigations of the specimen edges were performed to document the damage occurrence and to identify typical damage patterns.

The second step of this work was to develop an analytical methodology to accurately predict the damage onset observed during the experiments. All three load cases were analyzed using a detailed two-dimensional plane-strain finite element model. Both linear and geometrically nonlinear simulations were performed. As suggested in previous studies [2-4], a stress analysis was used to predict the location and orientation of the first transverse crack based on the principal transverse tension stress distribution.

The third step emphasized the use of a fracture mechanics approach to determine when a delamination would grow from the transverse cracks. This approach had been discussed in earlier studies [3, 4]. Delaminations of various lengths were simulated in two locations where delaminations were observed during the tests. Mode I and mode II strain energy release rate contributions, G_{I} and G_{II}, were calculated for all load cases using the virtual crack closure technique [9, 10] and compared to existing mixed-mode fracture toughness data.

EXPERIMENTAL INVESTIGATION

MATERIALS AND SPECIMEN PREPARATION

The specimens tested in this investigation consisted of a bonded skin and flange assembly as shown in Figure 1. Previous results had shown that the skin bending stiffness has a strong influence on the failure load. Therefore, the specimens were designed to have nearly the same bending stiffness D_{11} as those used in the previous monotonic and fatigue tests [2-5]. All

specimens were machined from the same panels. The skin lay-up, consisting of 14 plies, was $[0/45/90/-45/45/-45/0]_s$ and the flange lay-up, consisting of 10 plies, was $[45/90/-45/0/90]_s$.

Both skin and flange were made from IM6/3501-6 graphite/epoxy prepreg tape with a nominal ply thickness of 0.188 mm. First, the flange and skin laminates were cured separately. The flange parts were then cut into 50.0 mm long strips. A previous investigation had indicated that the angle at the flange tip has a significant influence on the strength [2]. A 20° taper angle was suggested in a previous investigation, however, incidentally a 27° taper was machined along the edges. It was assumed that the slight difference in taper angle would not have a significant effect on the failure behavior. Further, all specimens in the current investigation had the same taper angle, which would also be accounted for in the finite element model. Subsequently, the flange was adhesively bonded to the skin using a 177 °C cure film adhesive from American Cyanamid (CYTEC 1515). A grade-5 film was used to yield a nominally 0.127-mm thick bondline. However, because some of the adhesive flowed outwards during cure, the bondline thickness averaged 0.102 mm. A diamond saw was used to cut the panels into 25.4-mm wide by 203.2-mm long specimens. The specimen length is the only difference to previous studies in which specimens used for three-point and four-point bending tests were 127.0 mm long [2, 3, 5]. In the current study, the additional length is required only to mount the specimens in the grips for tension and combined tension/bending loading. Each specimen was then equipped with two strain gages, one located in the center of the flange and the other located on the skin as close to the flange tip as possible (Figure 1). Ply properties and adhesive material properties were measured at Boeing and are part of the standard design database for the V-22 tilt-rotor aircraft. Typical material properties for the composite tape and the adhesive material as taken from reference 2 are summarized in Table 1.

EXPERIMENTAL PROCEDURE

A total of five tension tests were performed in a servohydraulic load frame in displacement control. The actuator speed was controlled at 0.4 mm/min. The specimens were mounted in hydraulic grips to give a gage length of 127.0 mm as shown in Figure 2. An extensometer with a 25.4 mm gage length was mounted on the backside of the specimen and centered on the flange tip as shown in Figure 2. The tests were terminated when the flange debonded unstably from one of the flange tips.

Five bending tests were performed in a servohydraulic load frame at a monotonic rate of 1.52 mm/min. A photograph of the three-point bending test fixture is shown in Figure 3. The configuration used was similar to the one used in previous studies [2, 5]. The bottom support had a 127.0 mm span. Mid-span deflections were recorded using a spring loaded direct current

displacement transducer (DCDT) contacting the center of the flange as shown in Figure 3. The tests were stopped after the flange debonded unstably to the center of the specimen.

Tests under combined membrane and bending loading conditions were performed in the axial tension and bending (ATB) servohydraulic load frame shown in Figure 4. In this ATB load frame designed at the NASA Langley Research Center, the axial load cell is incorporated in the top grip that rotates with the upper specimen part (see close-up in Figure 5) [7, 8]. The specimens were mounted into the machine with great care placed on correct alignment of the specimen and the top grip/load cell set-up. The specimens were initially preloaded in load control to an axial tension load of 17.8 kN, which is 85% of the average damage initiation load determined for the tension test. While maintaining this preload, a transverse bending load was then applied in displacement control until flange debonding occurred. Maximum specimen deflections at the top grip contact point were recorded using a spring loaded linear variable differential transformer (LVDT).

The first specimen was tested with a gage length of 127.0 mm. The transverse load was applied at a constant rate of 1.52 mm/min (in accordance with three-point bending tests). As the stroke was increased, the specimen failed near the lower grip without evidence of flange debonding. As a result, the gage length was reduced to 101.6 mm for the four remaining specimens. The shortening allowed the lower flange tip to be closer to the bottom grip which increased the bending moment at the lower flange tip so that flange debonding occurred before skin failure. The transverse displacement rate was tripled to 4.57 mm/min to reduce testing time caused by the large specimen deflections necessary for damage initiation.

TEST RESULTS

In Figures 6 to 11, typical results of each test are shown as plots of load versus displacement or strain versus load. Results from finite element analyses, which are included in the figures, will be discussed later. For each loading configuration, the plots of load versus displacement and strain are from the same specimen. The strain-load curves are shown for flange strain and skin strain. The loads, flange and skin strains are reported in Tables 2 and 3 (tension and three-point bending tests) for the point of possible damage initiation as well as for the flange debond load. In Table 4 (ATB tests), the results are presented for the flange debond load only, since no damage initiation prior to failure was observed in these tests.

For tension specimens, the load-displacement curves were slightly nonlinear over a wide range as shown in Figure 6. Possible damage initiation was assumed when a small initial load drop was observed prior to flange debonding. At this point, a crack in one flange tip or even a small delamination along one flange corner was observed. In one specimen, no initial load drop or visible damage could be detected prior to flange debond. In general, the initial load drop occurred

above 90% of the flange debond load. Figure 7 shows the slightly nonlinear strain-load response until flange debonding. In all specimens, a load drop was also accompanied by a decrease in strain.

Typical plots for the three-point bending tests are shown in Figures 8 and 9. The load versus mid-span deflection curves of all three-point bending specimens showed nonlinear behavior at higher loads indicating possible damage initiation. Sometimes this behavior was accompanied by a minor load decrease (see Figure 8). However, no cracks or delaminations could be observed prior to ultimate flange failure. In all specimens, the nonlinearity or initial load decrease was again detected above 90% of the flange debond load. Both skin and flange strains showed linear behavior before flange debonding (see Figure 9). No decrease in load or strain was observed on the strain-load response prior to flange debonding.

In contrast to tension and three-point bending tests, the transverse load versus transverse displacement curves obtained from the ATB tests showed no indication of damage formation until just prior to skin failure for all specimens. Flange debonding could not be identified from these plots. A typical example is shown in Figure 10. Figure 11 shows a characteristic strain versus transverse load response starting from the strain caused by the axial load. Although Figure 11 shows linear behavior, the strain curves in some specimens deviated slightly from linearity prior to flange debonding. Flange debonding as detected during the experiments always occurred at maximum flange strain and was sometimes accompanied by a drop in skin strain. Results from finite element analyses, which are included in the figures, will be discussed later.

MICROSCOPIC INVESTIGATION

Photographs of the polished specimen edges were taken under a light microscope after testing was completed to document the occurrence of matrix cracks and delaminations. Damage was documented based on location at each of the four flange corners identified in Figure 12(a). Corners 1 and 4 and corners 2 and 3 had identical damage patterns. Typical damage patterns which were similar for all three loading configurations are shown in Figures 12(b) and (c). These drawings are based on the micrographs taken after the tests. Figure 13 presents two such photomicrographs for a three-point bending specimen. In general, failure in tension and three-point bending specimens occurred on one flange tip only, with no clear preference for either flange tip. Due to the moment distribution resulting from the loading and boundary conditions of the ATB test, failure in the ATB specimens occurred at the flange tip with the higher bending moment only, i.e., the flange tip closer to the lower grip.

At corners 1 and 4, a delamination running in the 90°/45° flange ply interface (delamination A) initiated from a matrix crack in the 90° flange ply as shown in Figure 12(b). At longer

delamination lengths, new matrix cracks formed and branched into both the lower 45° as well as the upper 90° flange ply. However, no branching into the adhesive bondline was observed.

At corners 2 and 3 a matrix crack formed at the flange tip in the 90° flange ply that subsequently ran through the lower 45° flange ply and the bondline into the skin. Subsequently, a split (delamination B1) formed from the tip of that matrix crack within the top 0° skin ply as depicted in Figure 12(c). In some cases, a second delamination (delamination B2) was observed below the first in the top 0°/45° skin ply interface. Both delaminations were present over a long distance until delamination B1 stopped and delamination B2 continued.

ANALYTICAL INVESTIGATION

FINITE ELEMENT ANALYSIS

The finite element (FE) method was used to analyze the test specimens for each loading case. The goal of this investigation was to study damage initiation using a stress analysis and the potential for delamination propagation using a fracture mechanics approach. FE models for one undamaged and two damaged specimens were developed and loads and boundary conditions were applied to simulate the three load cases. The two-dimensional cross section of the specimens was modeled using eight-noded quadrilateral plane strain elements using quadratic shape functions and a reduced (2x2) integration scheme. The models are shown in Figures 14 and 15. For the entire investigation, the ABAQUS® geometric nonlinear analysis procedure was used [11]. For the tension and three-point bending loading cases, the results of linear analyses were compared to those of nonlinear analyses. For the ATB test, only the ABAQUS® nonlinear solution was used since this allowed the axial load to rotate with the specimen as it deformed under the transverse load and accounted for the membrane stiffening effect caused by the axial load.

For the model of the undamaged specimen, a refined mesh was used in the critical area of the 90° flange ply where cracking was observed in the test specimens. An outline and two detailed views of the mesh are shown in Figure 14. Outside the mesh refinement area, all plies were modeled with one element through the ply thickness. In the refined region, two elements were used per ply thickness except for the first three individual flange plies above the bondline and the skin ply below the bondline which were modeled with four elements. Three elements through the thickness were used for the adhesive film. The described model provided adequate detail and consisted of 6492 elements and 19975 nodes and had 39888 degrees of freedom. The properties used to simulate the behavior of the graphite/epoxy material and the adhesive were measured at Boeing and are part of the standard design database for the V-22 tilt-rotor aircraft. Typical properties as taken from reference 2 are summarized in Table 1.

Based upon the experimental observations shown in Figures 12 and 13, a "damaged" model was also developed that included discrete matrix cracks and delaminations. The mesh described for the undamaged specimen was also used for this model, except for the critical area around the flange tip where delaminations were modeled as shown in Figure 15(a) for corners 1 and 4 and Figure 15(b) for corners 2 and 3. The initial matrix crack was modeled perpendicular to the flange taper. Damage was modeled at one flange tip only as shown in Figure 15. The deformed configurations are shown in Figure 15 to illustrate the modeling of discrete matrix cracks and delaminations. At the opposite taper, the mesh used in the model of the undamaged specimen was employed. This procedure was used to simulate the occurrence of damage onset only. In order to keep the FE mesh simple and avoid skewed elements, the split in the 0° ply (marked as "Delamination B1" in Figures 12(c) and 13(b)) was modeled as a delamination propagating between the adhesive film and the top 0° ply of the skin (Figure 15(b)). It is assumed that this slight alteration in geometry does not significantly influence the computed energy release rates. For the prediction of delamination growth, the fracture toughness values obtained from standard specimens with unidirectional layup were used as described below. It is inherent to a two dimensional plane strain FE model that the geometry, boundary conditions and other properties are constant across the entire width of the model. This may not always capture the true nature of the problem. As shown in Figures 12 and 13, the delamination pattern changed from corner 3 to corner 4 from a delamination running in the 90°/45° interface to a delamination propagating between the adhesive film and the top 0° ply of the skin. These three dimensional patterns of matrix cracks and delaminations which vary across the width of the specimen can not be accounted for in the current simple two dimensional plane strain FE model.

The schematics of the specimen, boundary conditions, and load cases applied in the simulations are shown in Figure 16 for the tension and three-point bending cases and in Figure 17 for the combined tension and bending case. For the tension and bending case, the mean loads reported for the point of damage initiation in Tables 2 and 3 were applied. At this point, matrix cracks are likely to form. For the simulation of the combined tension and bending loads in the ATB test, the top grip, the load cell, and the load pin were also modeled using three-noded quadratic beam elements as shown in Figure 17. A rectangular beam cross section was selected to model the square cross section of the top grip (I=1.87x10^6 mm^4) and load pin (I=1.4x10^6 mm^4) and a circular beam cross section was used to model the cylindrical load cell (I=8.37x10^3 mm^4). The beams were connected to the two-dimensional plane strain model of the specimen using multi-point constraints to enforce appropriate translations and rotations [11]. As shown in Figure 17, nodes 1-29 along the edge of the plane strain model (x =101.6 mm) were constrained to move as a plane with the same rotation as beam node A. To be consistent with the ATB tests, a constant axial load, P, was applied in a first load step while transverse loads remained zero. In a second load step, the axial

load was kept constant while the load orientation rotated with the specimen as it deformed under the transverse load. During the tests, the maximum specimen deflections under the transverse load were recorded at the top grip contact point. In the FE simulation a prescribed displacement, v, was applied which corresponded to the mean of transverse stroke (31 mm) reported in Table 4. For the beam model of the steel parts (top grip, load cell, and load pin), a Young's Modulus of 210 GPa and a Poisson's Ratio of 0.3 were used as material input data.

The Virtual Crack Closure Technique (VCCT) described in references 9 and 10 was used to calculate strain energy release rates for the delaminations. The mode I and mode II components of the strain energy release rate, G_I and G_{II}, were calculated as

$$G_I = -\frac{1}{2\Delta a}\left[Y'_i\left(v'_m - v'_{m^*}\right) + Y'_j\left(v'_\ell - v'_{\ell^*}\right)\right] \quad (1)$$

and

$$G_{II} = -\frac{1}{2\Delta a}\left[X'_i\left(u'_m - u'_{m^*}\right) + X'_j\left(u'_\ell - u'_{\ell^*}\right)\right] \quad (2)$$

where Δa is the length of the elements at the crack tip, X_i' and Y_i' are the forces at the delamination tip at node i, and u_m' and v_m' are the relative displacements at the corresponding node m behind the delamination tip as shown in Figure 18. Similar definitions are applicable for the forces at node j and displacements at node ℓ. Both forces and displacements were transformed into a local coordinate system (x', y'), that defined the normal and tangential coordinate directions at the delamination tip in the deformed configuration. The total strain energy release rate, G_T, was obtained by summing the individual mode components as

$$G_T = G_I + G_{II}. \quad (3)$$

The mode III component is zero for the plane strain case. The data required to perform the VCCT in equations (1) to (3) were accessed from the ABAQUS® result file. The calculations were performed in a separate post processing step using nodal displacements and nodal forces at the local elements in the vicinity of the delamination front.

ANALYSIS RESULTS

Global Response

First, the global response of the specimens was computed at load levels corresponding to the damage initiation loads observed in the experiments. The load-displacement and the load-strain

behavior computed for all three load cases were compared to the corresponding experimental results. This global response was used to examine whether the FE model, the boundary conditions, the load cases and the material properties used in the model were accurate. Note that the experimental data only represent one typical specimen, thus not accounting for any experimental scatter. Displacements were reported at the locations where they were taken in the experiments. Strains were computed at a single location corresponding to the center of the strain gage. A schematic of the deformed geometries, the boundary conditions, and the load cases applied in the simulations are shown in Figure 19 for all three load cases.

In the schematic of the deformed FE tension model in Figure 19(a), the elongation of the specimen caused by the applied tensile load is shown along with the bending effect caused by the load eccentricity. The load versus displacement plot in Figure 6 shows that the linear and nonlinear FE simulations are in good agreement. Moreover, there is very marginal difference between the analyses and the experiments, the model therefore accurately captured the global response. In Figure 7, a comparison of measured strains and computed results is shown. The strain-load responses for the skin are again in good agreement between the experiments and both analyses. For the flange strains the nonlinear analysis yielded results which were in agreement with the experiments. Strains obtained from the linear analysis were very low. Hence, a geometrically nonlinear FE analysis is necessary to account for the effects due to the load eccentricity in the flange region, the asymmetric layup with respect to the neutral axis and the membrane stiffening effect.

In the three-point bending test, the vertical displacement at the flange tip (Figure 3) was of the order of the skin thickness for the load level investigated. Hence, a geometrically nonlinear FE solution procedure may also be needed in this case. Both linear and nonlinear analyses were performed and computed displacements and strains were compared. The load-displacement plot in Figure 8 and the strain-load plot in Figure 9 show that both simulations and the experiments are within 10% of each other. Since the linear and nonlinear analyses are within 1%, a linear analysis is sufficient for the load level investigated, i.e., the mean load obtained form experiments for damage initiation. Higher load levels, however, might require a nonlinear analysis.

For the tension/bending loading case the load-displacement and strain-load plots in Figures 10 and 11 show that the nonlinear FE simulation and the experiments are within 20% of each other. A possible explanation for the stiffer response of the numerical model based on the difference in axial modulus measured in tension and bending is given in reference 12.

Local Response

The local response was studied in the critical area of the 90° flange ply where cracking was observed in the experiments. The goal of these FE analyses was to investigate damage initiation using a stress analysis and the potential for delamination propagation using a fracture mechanics approach.

The stress analysis was used to study the initial failure in the form of matrix cracks from which delaminations may start to grow. As shown in Figures 12 and 13, the first crack always occurred in the 90° flange ply closest to the skin. Results from previous investigations [2, 3] suggested that the local force and moment resultants, may be used to characterize damage onset. As shown in Figure 20, force and moment resultants per unit width were calculated from the normal stress σ_{xx} at the flange tip. Resultants were computed for damage initiation and flange debond load level based on stresses obtained from linear and nonlinear FE analyses. Results plotted in Figure 21 show that the three-point bending test is free of axial tension as the force resultants N_{xx} are zero as expected. A bending moment is present in the tension specimen caused by the load eccentricity in the flange region and the asymmetric layup of the combined skin and flange laminate with respect to the neutral axis. For the ATB test, calculated force and moment resultants lie between computed pure tension and pure bending values.

Earlier investigations [2, 3] also indicated that the maximum ply principal transverse tensile stress may cause the initial failure in the form of matrix cracks from which delaminations may start to grow. Failure, therefore, may occur when the computed principal tensile stress in the 2-3 plane of the ply (normal to the fiber direction) exceeds the transverse tensile strength of this ply. In this model, the ply 2-3 plane for a 90° ply coincides with the global x-y plane of the model. Maximum principal stresses can therefore be taken straight from the finite element results. The vector plot in Figure 22 shows the trajectories of the maximum principle tensile stresses in the flange ply. At the -45°/90° and 90°/45° interface, multiple vectors are displayed since the stresses were not averaged across boundaries for elements with different material properties. Comparing the trajectories in Figure 22 with the damage patterns shown in Figures 12 and 13 shows that the crack starts to grow perpendicular to the trajectory of the maximum principle tension stress. Computed maximum principal tension stresses σ_{max} in the elements with labeled element numbers in the 90° ply in Figure 22 are compared in Figure 23. For all three loading conditions, maximum principal tensile stresses computed for the damage initiation load level have similar magnitudes. Towards the center of the ply, principal stresses exceeded the failure strength of 61.1 MPa as found for a similar type of material (AS4/3501-6 in [13]) and hence ply cracks may develop. Consequently, the stress analysis based on the comparison of computed stresses with failure strengths appears to be an appropriate method to determine the location of the initial failure and the orientation of the resulting crack.

A fracture mechanics approach was used to investigate delamination growth once the initial crack had formed. It had been shown that care must be exercised in interpreting the values for G_I and G_{II} obtained using the virtual crack closure technique for interfacial cracks between two orthotropic solids [14, 15]. Therefore, it had been suggested to use element lengths Δa at the crack tip in such a manner that the computed results are insensitive to the variation of Δa. For practical applications the element size (length and height) should not be less than 1/10 of a ply thickness because the assumption that each ply can be modeled as a continuum is no longer valid. The element size at the crack tip also should not exceed the ply thickness as this requires smearing properties of individual plies. For the current investigation, the element length Δa was chosen to be 1/4 of the ply thickness for the delamination in the 90°/45° flange ply interface and 1/3 of the bondline thickness for the simulated propagation along the 0° skin ply/adhesive film interface.

The initial crack was modeled on one flange tip perpendicular to the flange taper as suggested by the microscopic investigation and the stress analysis described in the previous paragraph. Recall that the models of the discrete matrix cracks and delaminations are shown in Figure 15 in the deformed state. During the investigation, the delaminations were extended by adding new nodes at the crack tip and in front of the crack tip. These nodes were then assigned to the elements on one side of the crack thus creating a row of disconnected elements, which simulated the delamination as a discrete discontinuity. During a series of nonlinear finite element analyses, strain energy release rates were computed at each tip location for the flange debond load observed in the experiment. A simplified method was proposed in reference 16. In the current study, the delamination lengths, a, are measured from the end of the initial matrix crack as shown in Figure 15. For corners 1 and 4 (delamination in the 90°/45° flange ply interface), the delamination was extended to 0.6 mm which corresponds to a length where matrix crack branches were observed in the experiments as shown in Figures 12(b) and 13(a). The results are plotted in Figures 24 through 26 for all three loading conditions. Initial mode I and mode II values, computed at delamination onset (a = 0.034 mm, i.e., delamination length equal to the length of the first element as shown in Figure 15(a)), are similar for each type of test as shown in Table 5. In Figures 24 through 26, G_{II} for all load cases increases monotonically while G_I begins to level off.

For the simulated propagation along the 0° skin ply/adhesive film interface (corners 2 and 3) the delamination was extended to 1.6 mm. Plots of strain energy release rates computed for various delamination lengths are given in Figures 27 through 29. The computed values at delamination onset (a = 0.04 mm, i.e., delamination length equal to the length of the first element as shown in Figure 15(b)) are given in Table 6. Comparing all load cases, computed G_I results appear to have similar magnitudes. Mode II values, however, differ noticeably. As shown in Figures 27 through 29, at $a < 0.2$ mm the mode I contribution decreases with increasing

delamination length. The mode II contribution and the total strain energy release rate, however, increase with increasing delamination length. For $a > 0.2$ mm, the mode I contribution and the total strain energy release rate increase slowly with increasing delamination length for the bending load case mode and decrease slowly for the pure tension and the combined tension/bending load case. For all three load cases, the mode II contribution continues to increase at a much slower rate with increasing delamination length. The results discussed above will be used in a mixed-mode failure investigation to determine whether delamination onset and unstable propagation are possible at the applied loads where damage was observed in the experiments.

MIXED-MODE FAILURE INVESTIGATION

Accurate mixed-mode failure criteria are necessary for the prediction of delamination growth. A bilinear mixed-mode failure criterion was suggested in reference 17 for AS4/3501-6, a material similar to IM6/3501-6. The mixed-mode failure response was presented by plotting the mode I component of the mixed-mode fracture toughness versus the respective mode II component. A different approach to present the data was suggested in reference 18 where mixed-mode fracture toughness values, G_c, were plotted versus the mixed mode ratio G_{II}/G_T (see Figure 30). When this ratio is zero, G_c is simply the mode I fracture toughness, G_{Ic}. Alternatively, G_c becomes the mode II fracture toughness, G_{IIc}, when the mixed-mode ratio equals unity. An equation resulting from a least square regression cubic curve fit to these data defines the mixed-mode delamination fracture criterion for each ratio as:

$$G_c = 75.3 + 214.7\left(\frac{G_{II}}{G_T}\right) - 70.5\left(\frac{G_{II}}{G_T}\right)^2 + 327.4\left(\frac{G_{II}}{G_T}\right)^3 \qquad (4)$$

Hence, for a given mixed-mode ratio, growth is possible when the total mixed-mode strain energy release rate exceeds the critical value.

In the current study, computed total strain energy release rates, G_T, were compared to the critical value, G_c, for the appropriate mixed mode ratio (G_{II}/G_T) for each load case in order to determine the potential for delamination growth. Values calculated for delamination onset ($a = 0.034$ mm, i.e., delamination length equal to the length of the first element as shown in Figure 15(a)) in the 90°/45° flange ply interface are below the fracture toughness data as shown in Table 5. Consequently, onset is unlikely to occur at the load corresponding to damage initiation for all three tests. Propagation in the 0° skin ply/adhesive film interface, on the other hand, will occur in all three cases as the computed results for delamination onset ($a = 0.04$ mm, i.e., delamination length equal to the length of the first element as shown in Figure 15(b)) are much higher than the

reported fracture toughness values as shown in Table 6. It is important to recall that in the experiments the failure was observed as a split in the 0° ply as shown in Figures 12 (c) and 14 (b). This failure was modeled as a delamination propagating between the adhesive film and the top 0° ply of the skin as shown in Figure 15 (b) only in order to avoid skewed elements. Hence, for predicting growth of the split in the 0° ply it is appropriate to compare energy release rates computed for the 0° skin ply/adhesive film interface with fracture toughness values obtained from standard tests. Unstable propagation is likely since the calculated G_T-values remain above the mixed-mode fracture toughnesses over the entire simulated length as shown in Figures 27 to 29. This assumption is confirmed by the experimental results of this study.

The above findings suggest that once a matrix crack has formed, a delamination (delamination B1 from Figure 13) will also form and grow in an unstable manner between the adhesive film and the top 0° skin ply. The second delamination observed in the 90°/45° flange ply interface (delamination A from Figure 13) requires more energy to initiate than available at the load levels used in this FE analysis, i.e., the loads corresponding to possible matrix ply crack initiation. The energy for this second delamination may come from an increase in load or may be caused by an increase in G_T due to the presence of the first delamination in the 0° skin ply/adhesive film interface. These two possibilities are studied in detail in the following paragraphs. The response of the numerical model with respect to the difference in axial moduli measured in tension and bending is discussed in reference 12. This discussion includes the effect of a lowered axial modulus on computed strain energy release rates for specimens subjected to bending and combined tension/bending loading.

First, strain energy release rates were calculated at the flange debond load observed in the experiment. Results for the second delamination in the 90°/45° flange ply interface are included in Table 5. Strain energy release rates are higher, however, they still remain below the fracture toughness. This suggests that delamination growth is unlikely.

Second, the possibility of an increase in G_T due to the presence of the first delamination was investigated. On one flange side a delamination of 10 mm was simulated between the adhesive film and the top 0° skin ply as an initial disbond. This length was kept constant during the remainder of the investigation. At the opposite taper, the delamination in the 90°/45° flange ply interface was modeled as described in the previous paragraph. The model is shown in Figure 31. Again, the second delamination was extended to 0.6 mm which corresponds to a length where matrix crack branches were observed in the experiments. The total strain energy release rates computed at loads corresponding to possible damage initiation are plotted in Figure 32 for all three loading cases. The values computed previously for the condition without the assumed initial disbond (G_T from Figures 24 through 26) were included in Figure 32 for comparison. For both conditions, G_T increases monotonically with growing delamination length. For the tension and

combined tension/bending load case computed values are smaller for the condition where delamination formation was assumed between the adhesive film and the top 0° skin ply. The computed values at delamination onset (a = 0.034 mm, i.e., delamination length equal to the length of the first element as seen in Figure 31) are shown in Figure 33 for delamination onset and flange debond load. The values computed previously for the condition without the assumed initial disbond (G_T from Table 5) were included in Figure 33 for comparison. Values for both load levels are again below the fracture toughness data, which suggests that delamination growth in the 90°/45° flange ply interface is also unlikely in the presence of a 10 mm long delamination in the 0° skin ply/adhesive film interface. Based upon this study it can be concluded that delamination growth in the 90°/45° flange ply interface cannot be explained using strain energy release rates based on two-dimensional plane strain FE analyses. The observed three-dimensional pattern of matrix cracks and delaminations seen in the specimens could not be accounted for with the current simple two-dimensional plane strain FE model. A detailed investigation of the delaminated area should include a local three-dimensional analysis, which allows to model the changing failure patterns across the width of the specimen (as shown in Figures 12 and 13) more realistically. The three-dimensional model therefore would provide additional results with respect to failure interaction and its development across the width of the specimen.

CONCLUDING REMARKS

The damage mechanisms in composite bonded skin/stringer constructions under uniaxial and biaxial (in-plane/out-of-plane) loading conditions have been investigated using experimental and numerical approaches. A consistent step-wise approach was used based on experiments to observe the failure pattern, computational stress analysis to determine the location of first matrix cracking and computational fracture mechanics to investigate the potential for delamination growth. Tests were performed under monotonic loading conditions in tension, three-point bending, and combined tension/bending to evaluate the debonding mechanisms between the skin and the bonded stringer or frame. Microscopic investigations of the specimen edges showed that all tests yielded similar damage patterns. For all three load cases, failure initiated in the flange, near the flange tip, causing part of the flange to fully debond from the skin.

Based upon the experimental findings, a two-dimensional nonlinear plane-strain finite element (FE) analysis was performed using the ABAQUS® FE code. For tension and three-point bending tests, linear and geometrically nonlinear simulations were performed. Overall, both computed results were found to be in good agreement with the experimental data. To account for the large displacements observed in the ATB tests, only the geometrically nonlinear analysis was performed. Again, the results were in good agreement with the experiments.

A stress analysis was used to investigate the onset of failure. This approach showed that the location and orientation of the initial transverse ply crack in the flange are dependent on the stress distribution in the critical area near the flange tip. For all three loading conditions, computed maximum principal tensile stresses were almost identical and exceeded the transverse tension strength of the material. A fracture mechanics approach was used to determine the potential for delamination growth from the initial transverse crack. In this approach, delaminations of various lengths originating from the transverse crack as observed in the experiments were simulated. Mode I and mode II strain energy release rate contributions were calculated for all load cases using the virtual crack closure technique. Computed total strain energy release rates were compared to critical values obtained from an existing mixed-mode failure criterion. The results suggest that once a matrix ply crack has initiated in the flange, a delamination will form and grow in an unstable manner between the adhesive film and the top 0° skin ply as observed in the micrographs. A second delamination located in the 90°/45° flange ply interface requires more energy to initiate than was computed to be available at loads corresponding to possible damage initiation. Strain energy release rates calculated at the flange debond load observed in the experiment were higher than the initiation values but still remained below the fracture toughness. Computed values also remained below the fracture toughness data in the presence of a 10 mm delamination modeled in the 0° skin ply/adhesive film interface. Consequently, delamination growth in the 90°/45° flange ply interface cannot be explained using strain energy release rates computed from a two-dimensional plane strain FE analysis. A detailed investigation of the delaminated area should include a local three-dimensional analysis, which allows to model the changing failure patterns across the width of the specimen more realistically.

ACKNOWLEDGMENTS

This work was performed as part of a Cooperative Research and Development Agreement (CRDA) between the U.S. Army Research Laboratory, Vehicle Technology Directorate located at NASA Langley Research Center, and Boeing, Philadelphia.

REFERENCES

[1] Minguet, P. J., Fedro, M.J., O'Brien, T. K., Martin, R. H., Ilcewicz, L. B., Awerbuch, J., and Wang, A., "Development of a Structural Test Simulating Pressure Pillowing Effects in a Bonded Skin/Stringer/Frame Configuration," *Proceedings,* Fourth NASA/DoD Advanced Composites Technology Conference, Salt Lake City, UT, June 1993.

[2] Minguet, P. J. and O'Brien, T. K., "Analysis of Test Methods for Characterizing Skin/Stringer Debonding Failures in Reinforced Composite Panels," *Composite Materials: Testing and Design, Twelfth Volume, ASTM STP 1274,* August 1996, pp. 105-124.

[3] Minguet, P. J. and O'Brien, T. K., "Analysis of Composite Skin/Stringer Bond Failures Using a Strain Energy Release Rate Approach," Proceedings of the Tenth International Conference on Composite Materials, Vol. I, Woodhead Publishing Ltd., 1995, pp. 245-252.

[4] Minguet, P. J., "Analysis of the Strength of the Interface between Frame and Skin in a Bonded Composite Fuselage Panel," Proceedings of the 38th AIAA/ASME/ASCE/AHS/ASC SSDM Conference and Exhibit, Kissimmee, Florida, 1997, AIAA-97-1342, pp. 2783-2790.

[5] Cvitkovich, M. K., O'Brien, T. K., and Minguet, P. J., "Fatigue Debonding Characterization in Composite Skin/Stringer Configurations," *Composite Materials: Fatigue and Fracture, Seventh Volume, ASTM STP 1330,* 1998, pp. 97-121.

[6] Van Rijn, J.C.F.N., "Failure Criterion for the Skin-Stiffener Interface in Composite Aircraft Panels," *Proceedings of the ASC 13th Annual Technical Conference on Composite Materials,* 1998, pp. 1064-1093.

[7] O'Brien, T. K., Murri, G. B., Hagemeier, R., and Rogers, C., "Combined Tension and Bending Testing of Tapered Composite Laminates," *Applied Composite Materials,* 1, 1995, pp. 401-413.

[8] Murri, G. B., O'Brien, T. K., and Rousseau, C. Q., "Fatigue Life Methodology for Tapered Composite Flexbeam Laminates," *Journal of the American Helicopter Society,* Vol. 43, (2), April 1998, pp. 146-155.

[9] Rybicki, E. F. and Kanninen, M. F., "A Finite Element Calculation of Stress Intensity Factors by a Modified Crack Closure Integral," *Eng. Fracture Mech.,* 9, 1977, pp. 931-938.

[10] Raju, I. S., "Calculation Of Strain-Energy Release Rates With Higher Order And Singular Finite Elements," *Eng. Fracture Mech.,* 28, 1987, pp. 251-274.

[11] ABAQUS/Standard, "User's Manual, Volume II", Version 5.6, 1996

[12] Krueger, R., Cvitkovich, M. K., O'Brien, T. K. and Minguet, P. J., "Testing and Analysis of Composite Skin/Stringer Debonding Under Multi-Axial Loading", NASA/TM-1999-209097, February 1999.

[13] O'Brien, T. K. and Salpekar, S. A., "Scale Effects on the Transverse Tensile Strength of Graphite/Epoxy Composites," *Composite Materials: Testing and Design, Eleventh Volume,* ASTM STP 1206, 1993, pp. 23-52.

[14] Sun, C. T. and Manoharan, M. G., "Strain Energy Release Rates of an Interfacial Crack Between Two Orthotropic Solids," *Journal of Composite Materials*, Vol. 23, May 1989, pp. 460-478.

[15] Raju, I. S., Crews, J.H. and Aminpour, M.A., "Convergence of Strain Energy Release," *Eng. Fracture Mech.,* 30, 1988, pp. 383-396.

[16] Krueger, R., Minguet, P.J. and O'Brien, T.K., "A Method for Calculating Strain Energy Release Rates in Preliminary Design of Composite Skin/Stringer Debonding Under Multi-Axial Loading," NASA TM, 1999.

[17] Reeder, J. R., "A Bilinear Failure Criterion for Mixed-Mode Delamination," *Composite Materials: Testing and Design, Eleventh Volume,* ASTM STP 1206, 1993, pp. 303-322.

[18] O'Brien, T. K., "Composite Interlaminar Shear Fracture Toughness, G_{IIc}: Shear Measurement or Sheer Myth?," *Composite Materials: Fatigue and Fracture, Seventh Volume, ASTM STP 1330,* 1998, pp. 3-18.

TABLE 1. MATERIAL PROPERTIES.

IM6/3501-6 Unidirectional Graphite/Epoxy Tape [3]		
E_{11} = 144.7 GPa	E_{22} = 9.65 GPa	E_{33} = 9.65 GPa
ν_{12} = 0.30	ν_{13} = 0.30	ν_{23} = 0.45
G_{12} = 5.2 GPa	G_{13} = 5.2 GPa	G_{23} = 3.4 GPa

CYTEC 1515 Adhesive		
E = 1.72 GPa	ν = 0.30	(assumed isotropic)

TABLE 2. RESULTS FOR TENSION TESTS.

Specimen	Damage initiation load kN	Damage initiation flange strain με	Damage initiation skin strain με	Flange debond load kN	Flange strain at flange debond load με	Skin strain at flange debond load με
2	20.5	1225	5619	22.8	1348	6084
4	21.8	1419	6312	23.6	1231	6685
6	19.9	1185	5834	23.1	1187	6599
8	20.9	1300	6051	23.0	1115	6463
10	21.1	1360	6092	21.1	1360	6092
Mean	20. 9	1298	5982	22.7	1248	6385
Std. Dev.	0.7	96	264	0.9	105	282
CoV, %	3.3	7.4	4.4	4.2	8.4	4.4

TABLE 3. RESULTS FOR THREE-POINT BENDING TESTS.

Specimen	Damage initiation load kN	Damage initiation flange strain με	Damage initiation skin strain με	Flange debond load kN	Flange strain at flange debond load με	Skin strain at flange debond load με
11	404	3207	3811	440	3508	4160
13	433	3051	3691	484	3405	4110
15	445	3231	3659	468	3408	3868
17	425	3036	3657	434	3103	3701
19	431	3023	3481	488	3428	3945
Mean	428	3110	3660	463	3370	3957
Std. Dev.	14.9	101	118	24.4	155	186
CoV, %	3.5	3.2	3.2	5.3	4.6	4.7

TABLE 4. RESULTS FOR ATB TESTS.

Specimen	Flange debond load, kN	Stroke at flange debond load, mm	Flange strain at flange debond load, με	Skin strain at flange debond load, με
12	2.8	31.6	1318	7199
14	-	-	-	-
16	2.9	33.2	1232	7254
18	2.9	33.9	1276	7295
20	2.2	25.1	1278	7015
Mean	2.7	31.0	1276	7191
Std. Dev.	0.3	4.0	35	124
CoV, %	11.6	13.0	2.8	1.7

axial load = 17.8 kN

TABLE 5. RESULTS FOR DELAMINATION GROWTH IN 90°/45° INTERFACE.

Specimen	G_I, J/m^2	G_{II}, J/m^2	G_T, J/m^2	G_{II}/G_T	G_c, J/m^2
Tension*	53.4	13.3	66.7	0.200	118
Bending*	42.4	10.2	53.0	0.200	118
Tension$^+$	63.8	15.7	79.5	0.200	118
Bending$^+$	49.5	12.4	61.9	0.200	118
ATB$^+$	67.3	24.1	91.4	0.260	132

* results computed at damage initiation load $^+$ results computed at flange debond load

TABLE 6. RESULTS FOR DELAMINATION GROWTH IN FILM/0° INTERFACE.

Specimen	G_I, J/m^2	G_{II}, J/m^2	G_T, J/m^2	G_{II}/G_T	G_c, J/m^2
Tension*	362	76.8	439	0.175	112
Bending*	272	39.0	311	0.125	101
Tension$^+$	467	93.1	530	0.189	114
Bending$^+$	318	45.9	364	0.130	103
ATB$^+$	358	191	549	0.349	155

* results computed at damage initiation load $^+$ results computed at flange debond load

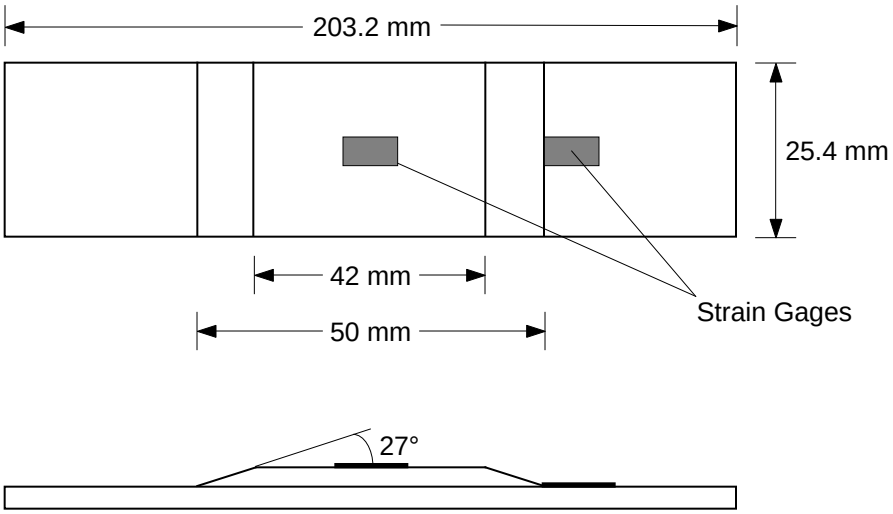

Figure 1. Specimen Configuration.

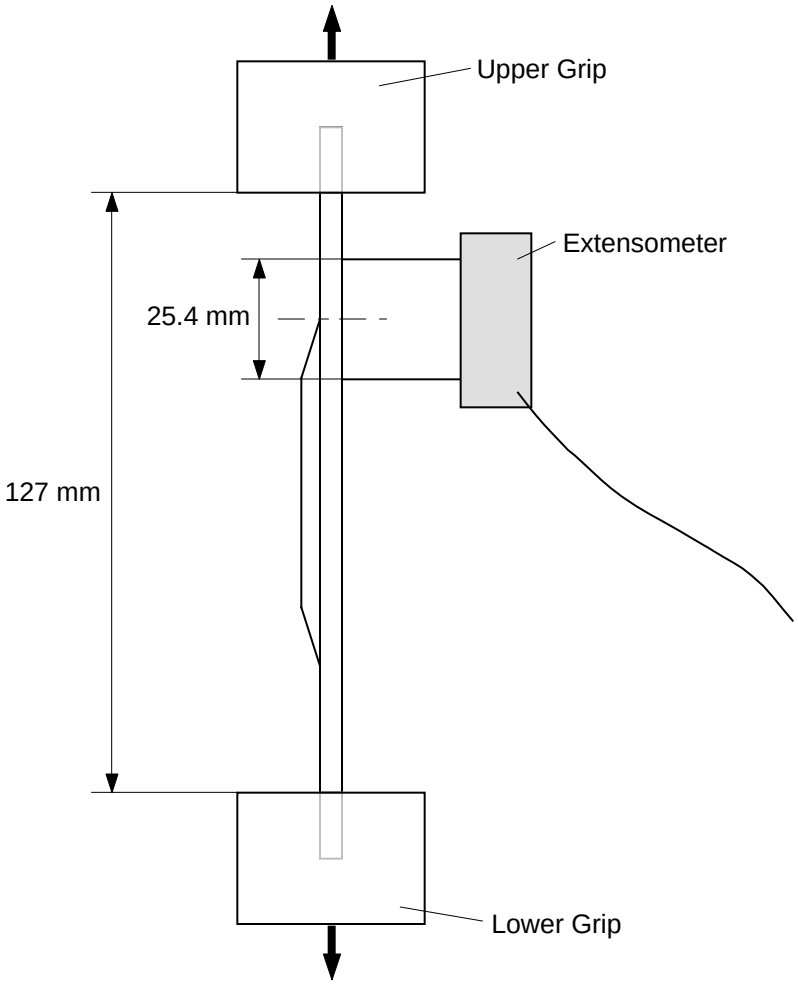

Figure 2. Tension Test Set-Up.

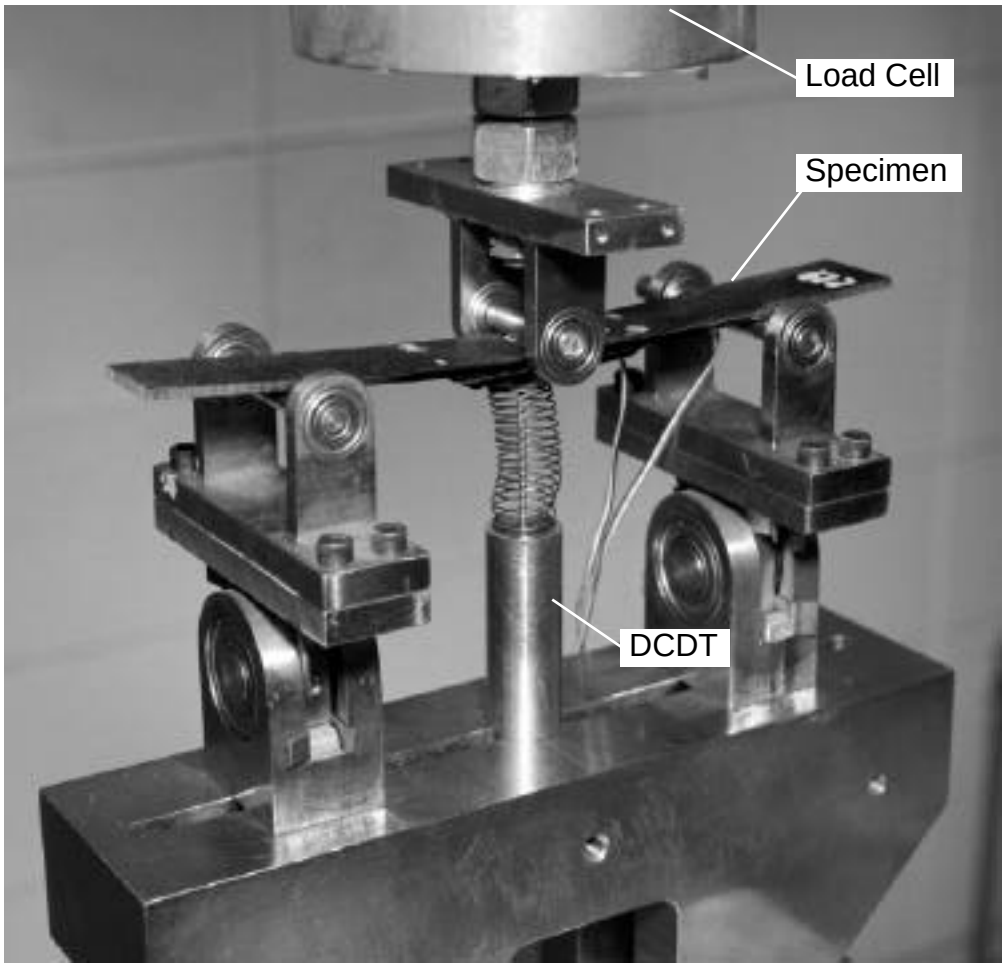

Figure 3. Three-Point Bending Test Set-Up.

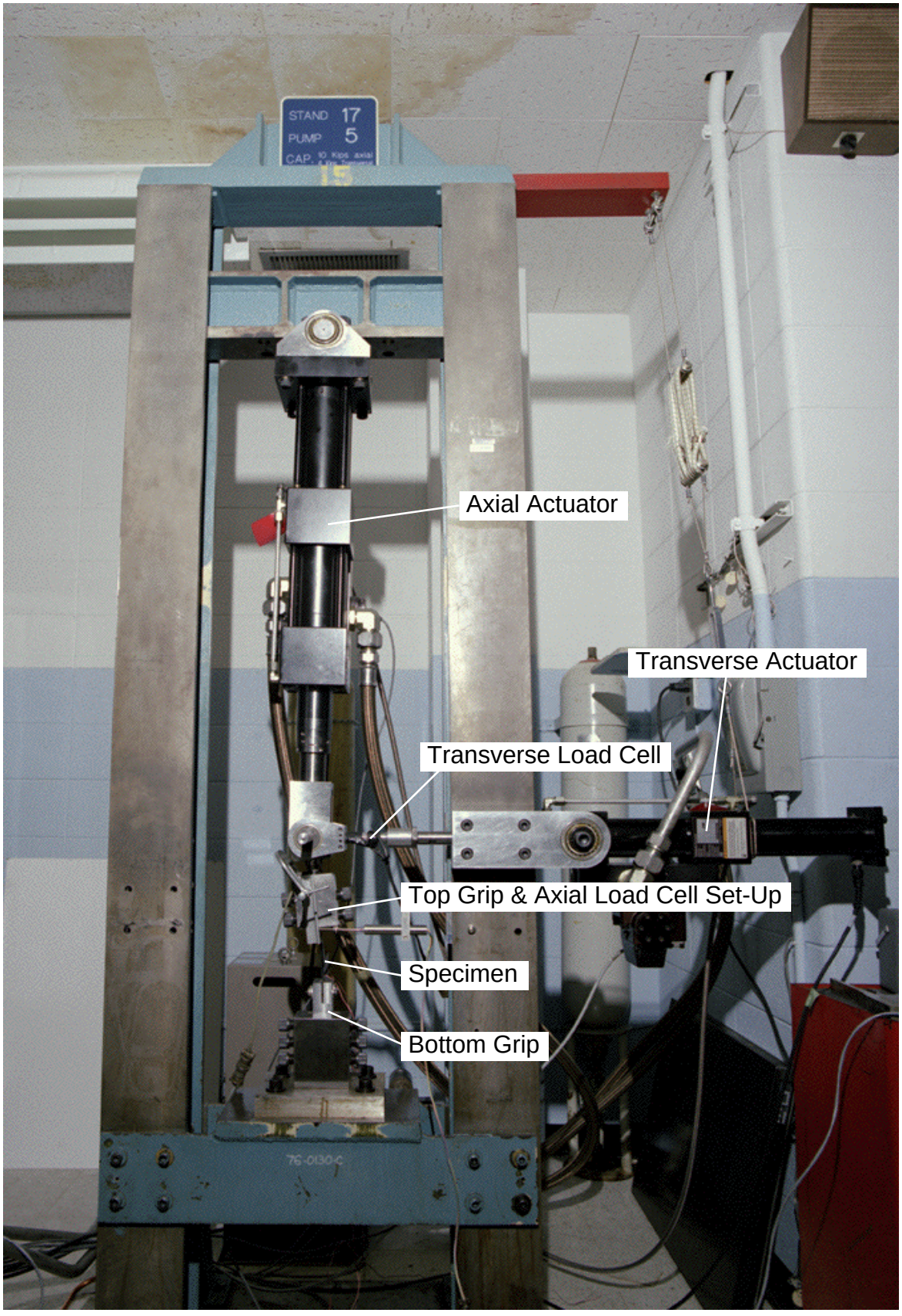

Figure 4. ATB Test Set-Up.

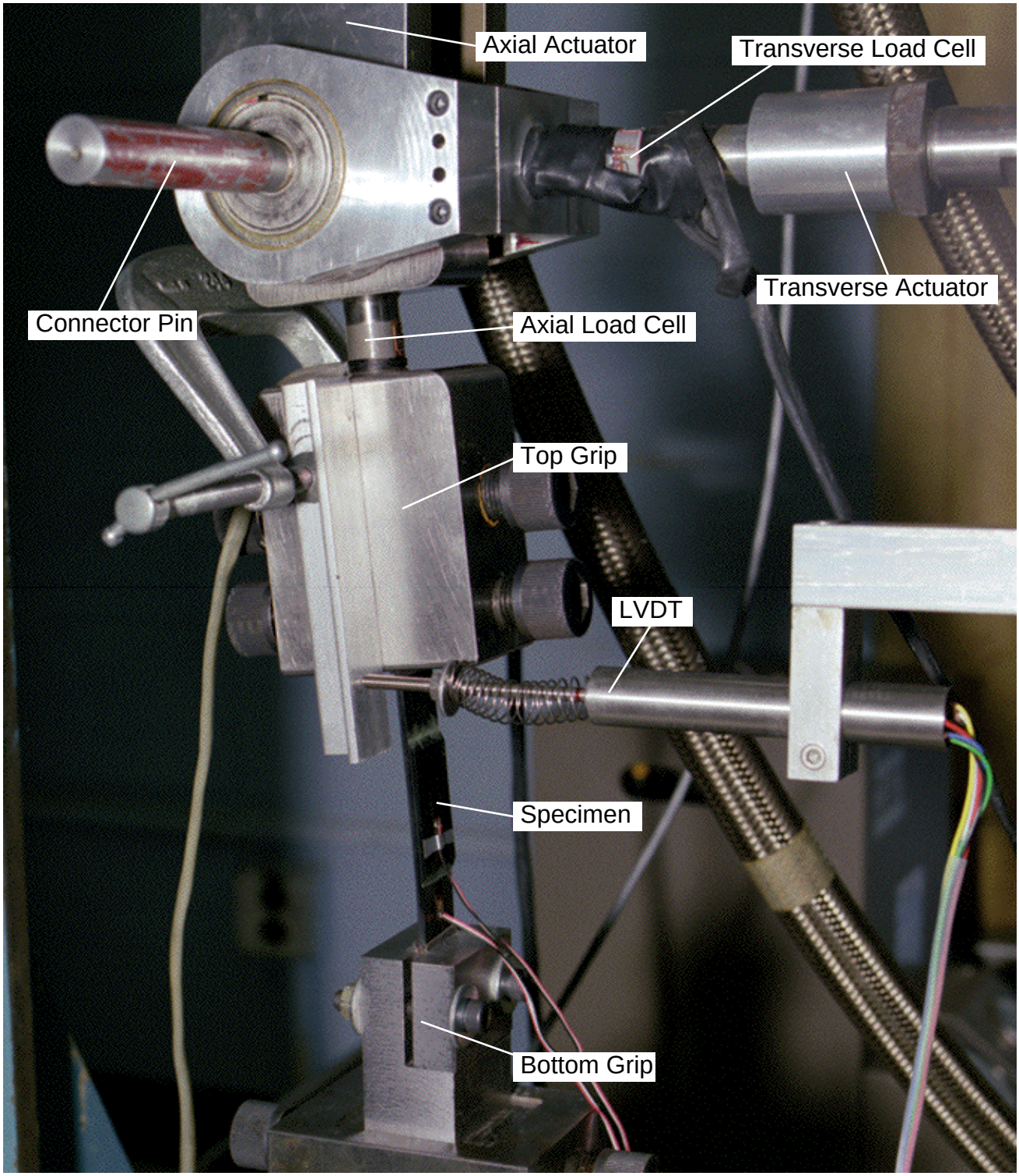

Figure 5. ATB Test Set-Up Close View.

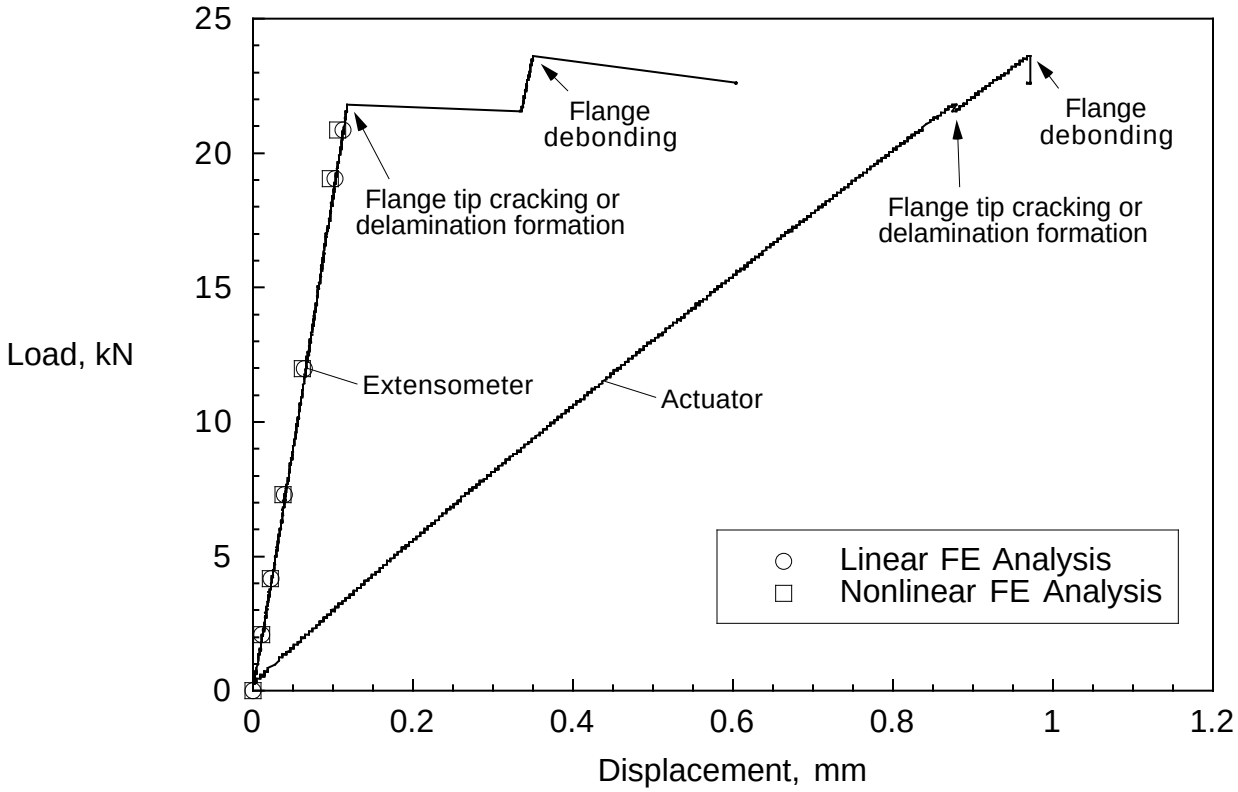

Figure 6. Typical Load-Displacement Plot for Tension Tests.

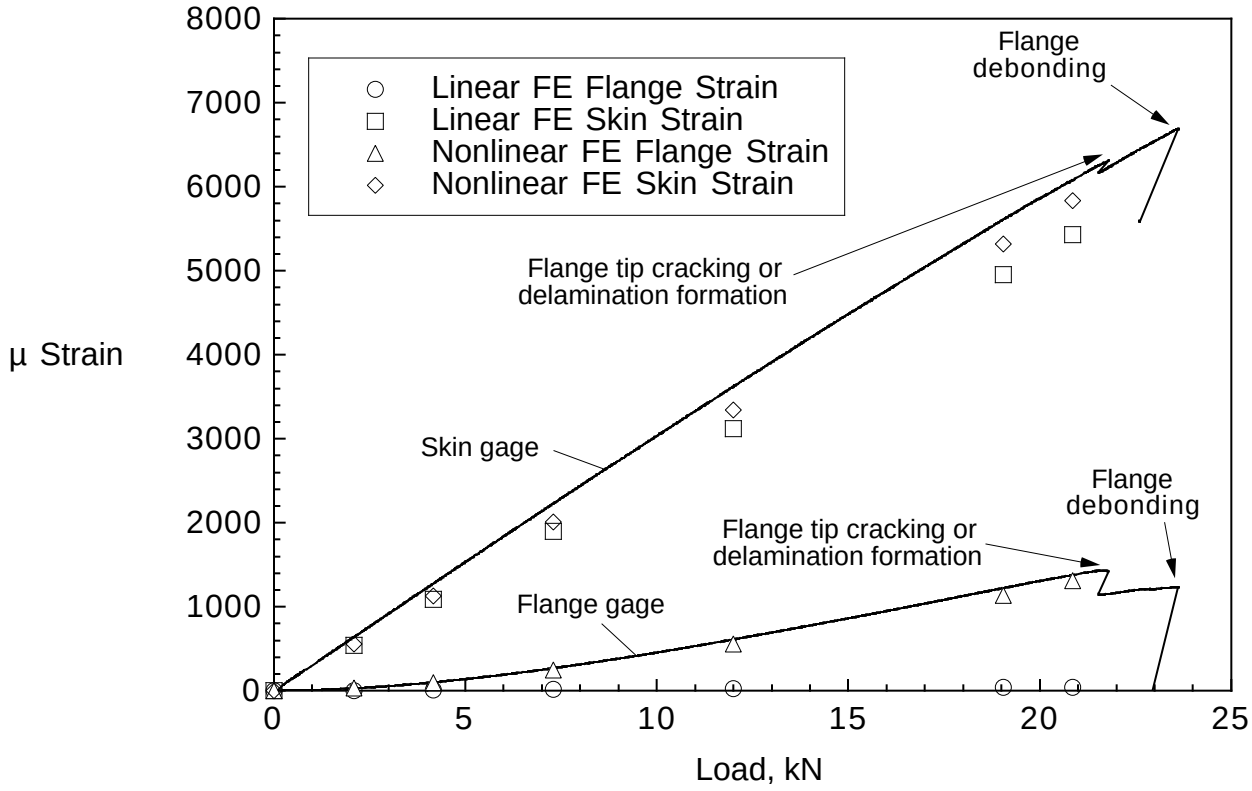

Figure 7. Typical Strain-Load Plot for Tension Tests.

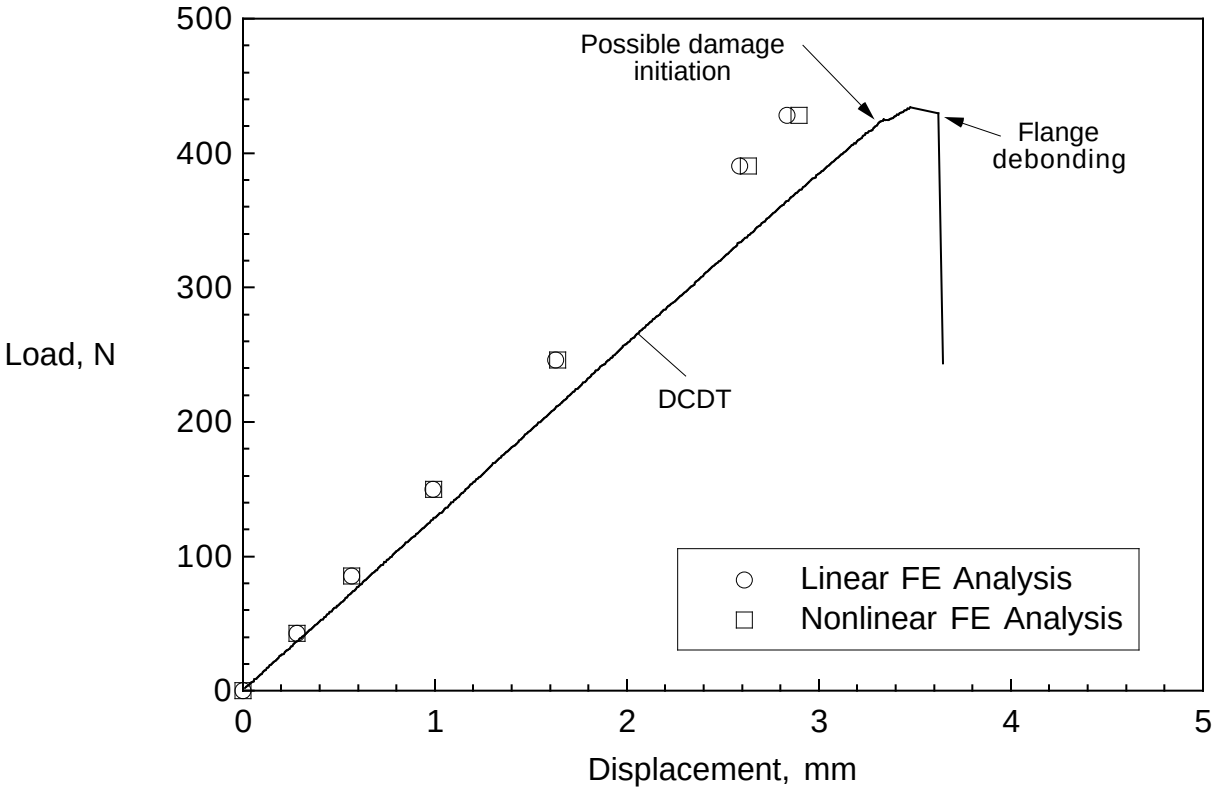

Figure 8. Typical Load-Displacement Plot for Three-Point Bending Tests.

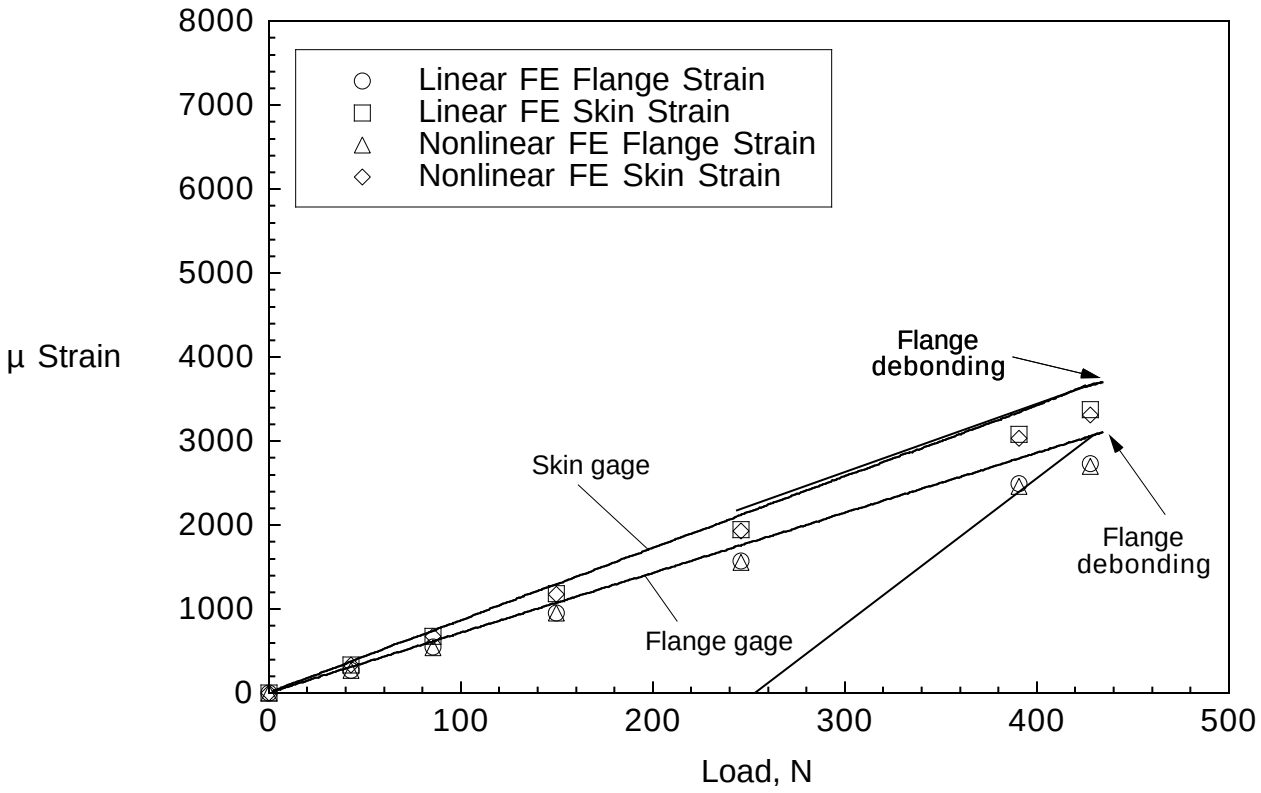

Figure 9. Typical Strain-Load Plot for Three-Point Bending Tests.

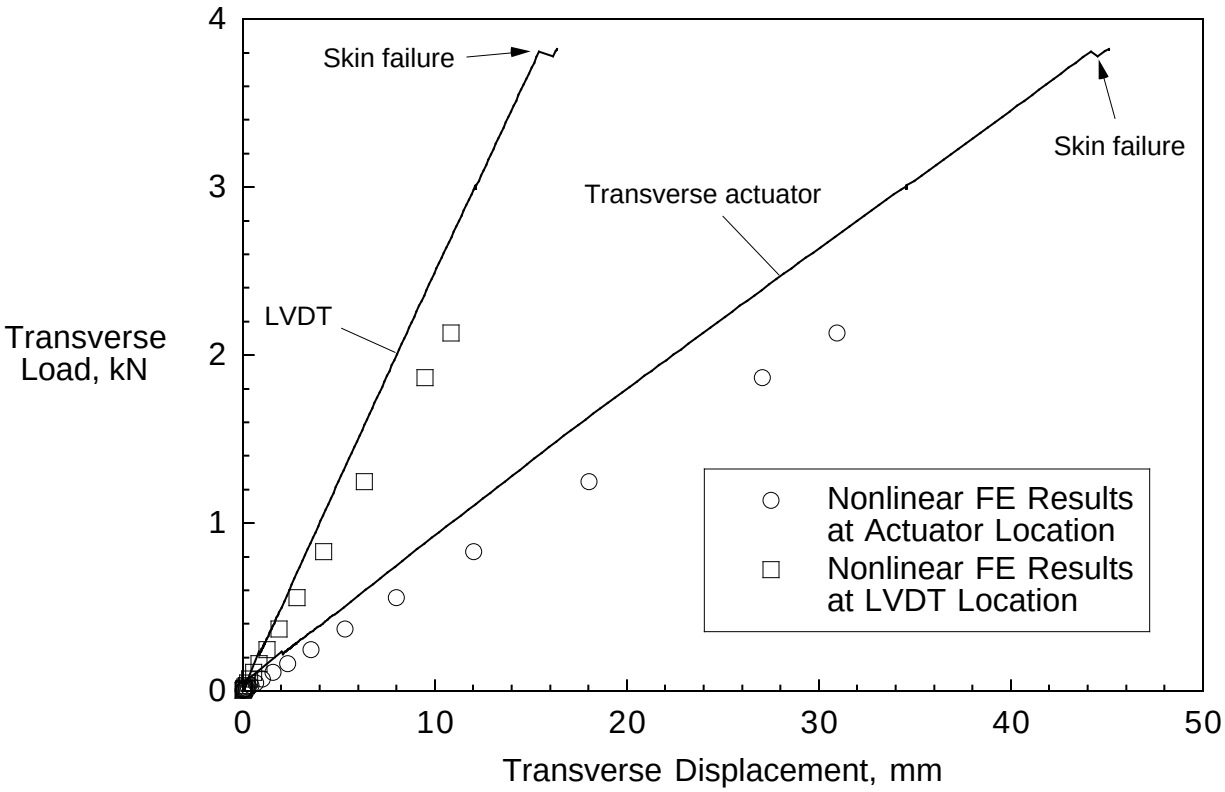

Figure 10. Typical Load-Displacement Plot for ATB Tests.

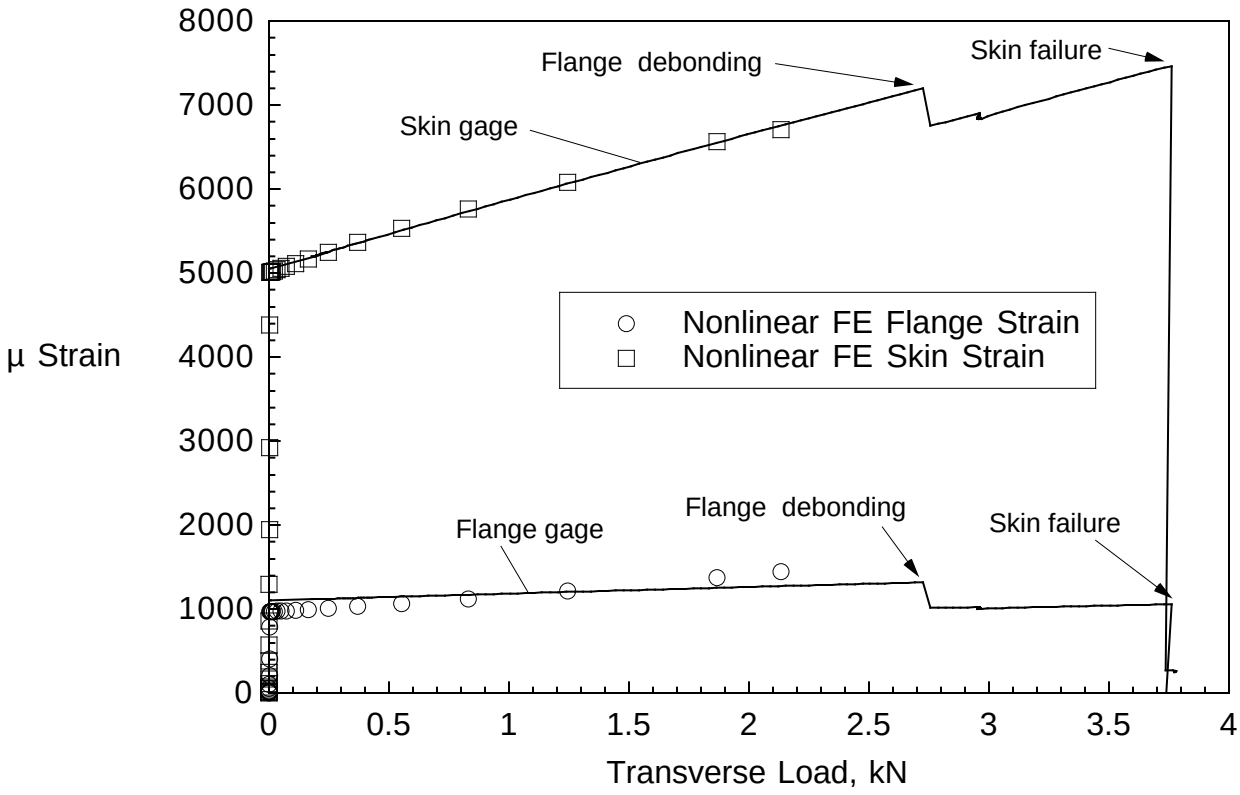

Figure 11. Typical Strain-Load Plot for ATB Tests.

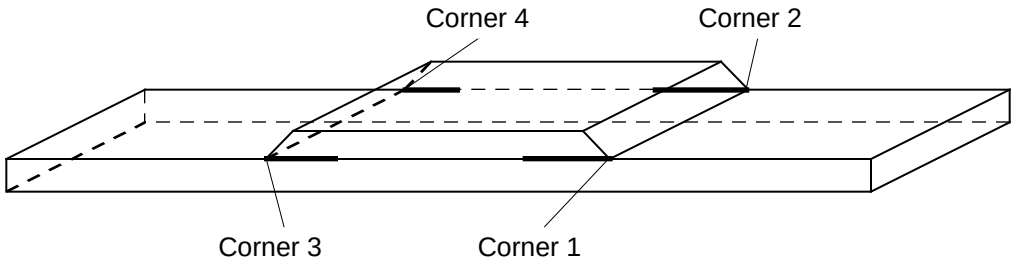

(a) Specimen with Crack Locations.

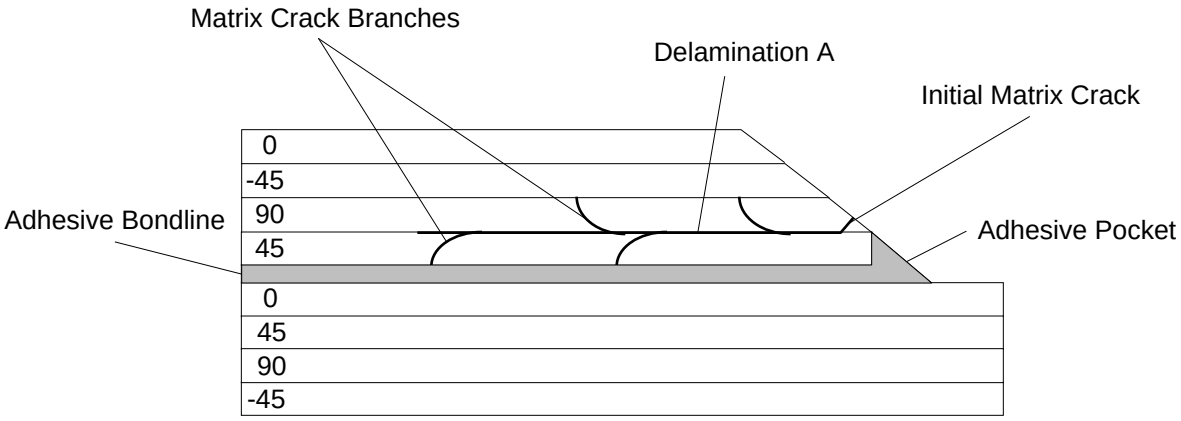

(b) Corners 1 and 4

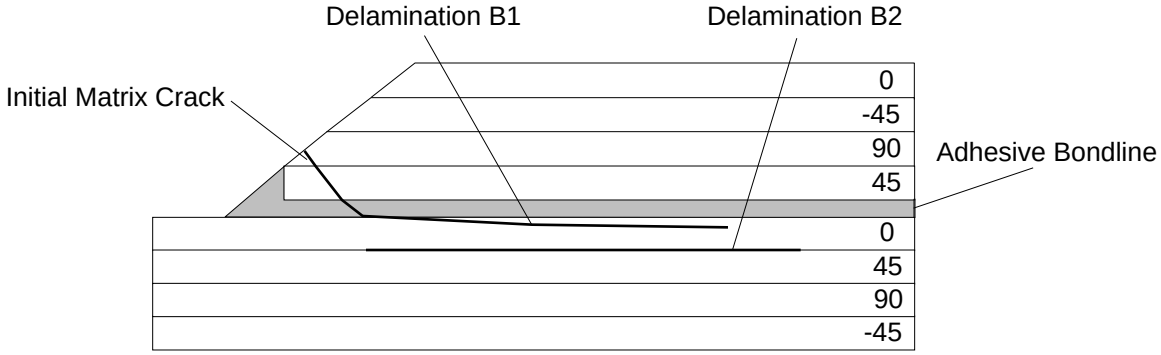

(c) Corners 2 and 3

Figure 12. Typical Damage Patterns.

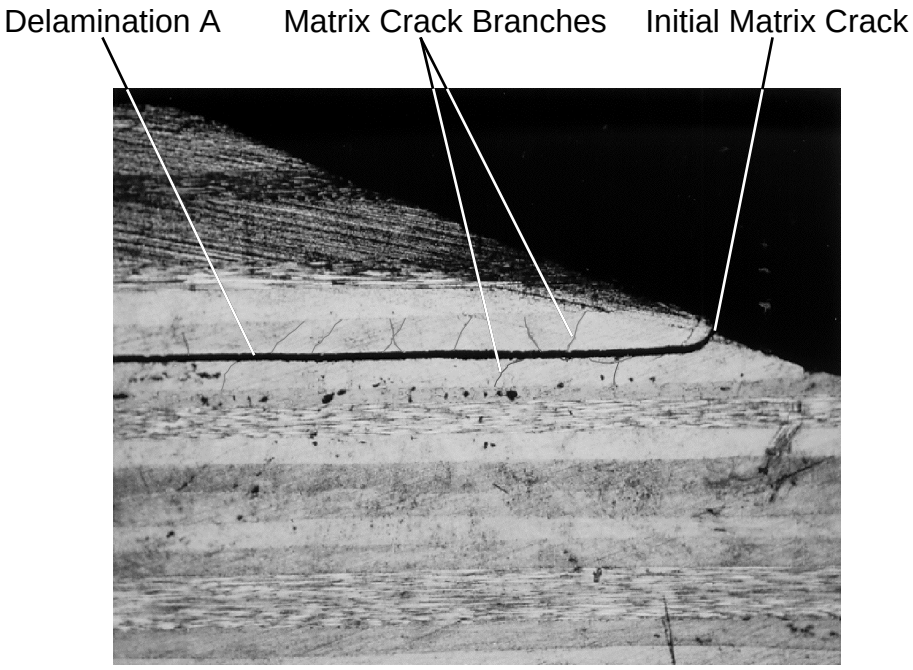

(a) Delamination A in the 90°/45° Flange Ply Interface at Corner 4

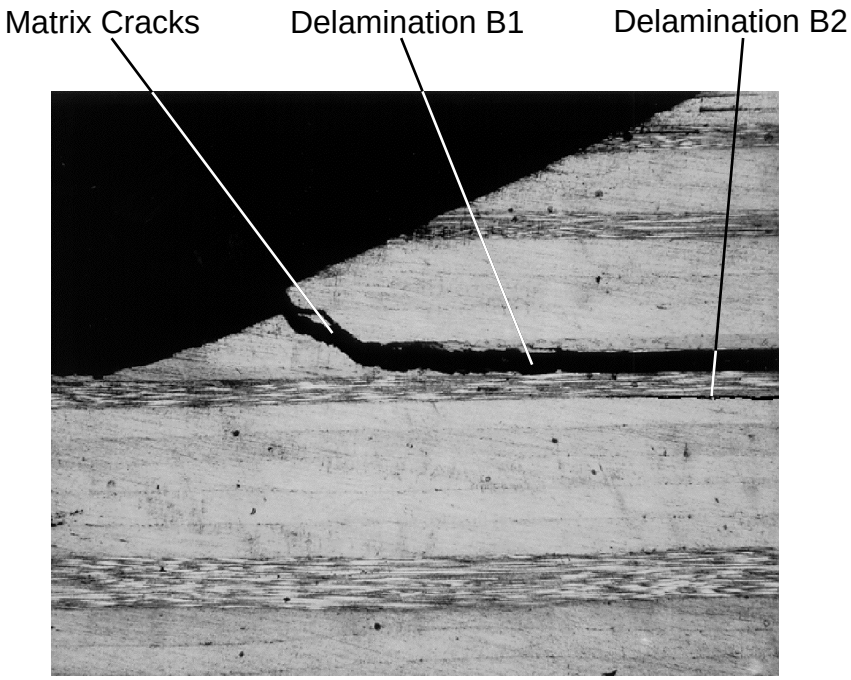

(b) Delamination B1 in the Top 0° Skin Ply and Beginning of Delamination B2 in The top 0°/45° Skin Ply Interface at Corner 2

Figure 13. Micrograph Showing the Side View of a Failed Three-Point Bending Specimen.

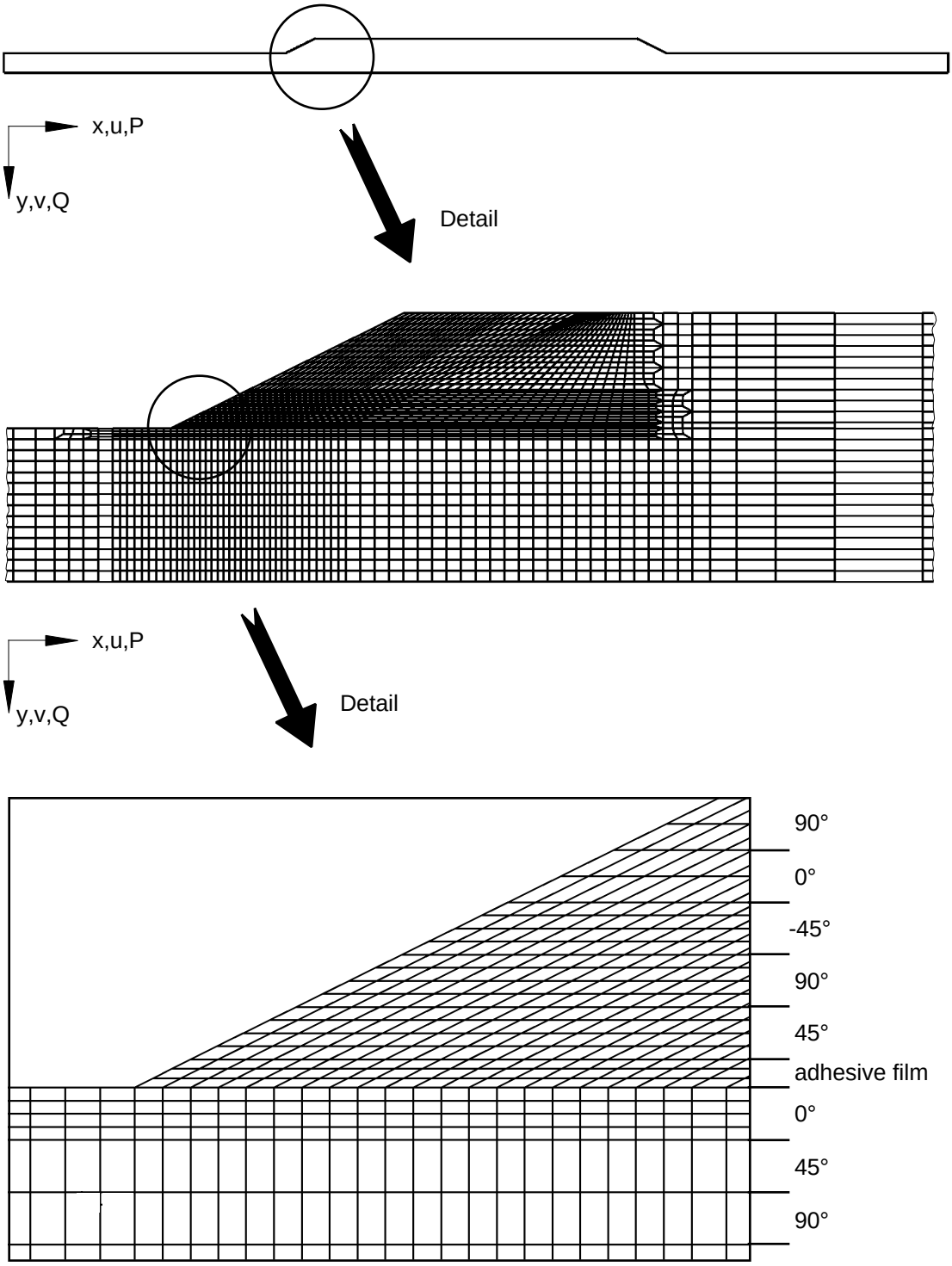

Figure 14. Finite Element Model of an Undamaged Specimen.

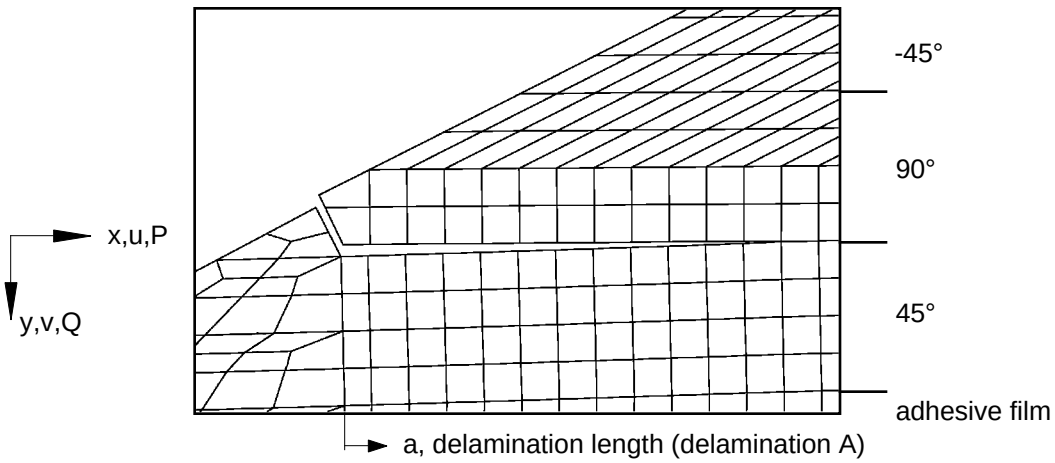

(a) Corners 1 and 4 (deformed geometry)

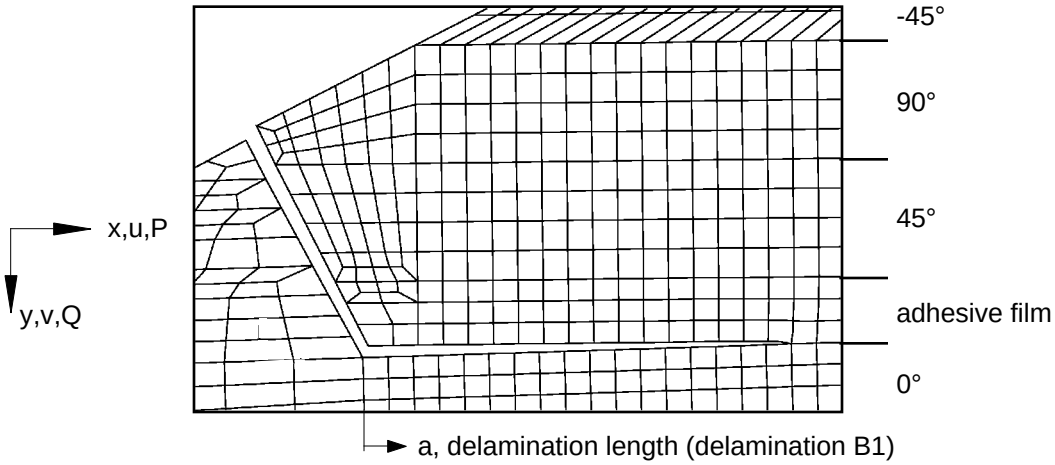

(b) Corners 2 and 3 (deformed geometry)

Figure 15. Modeled Damage Patterns.

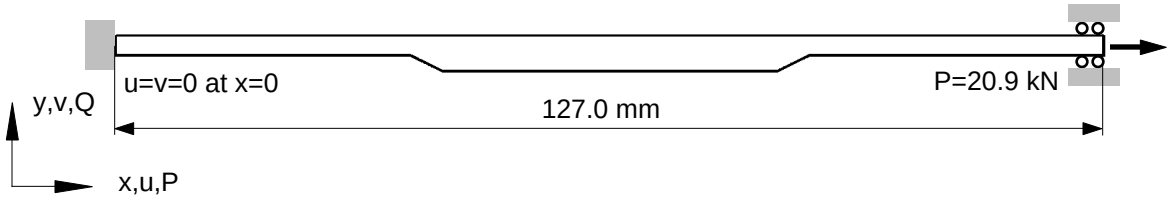

(a) Tension Specimen

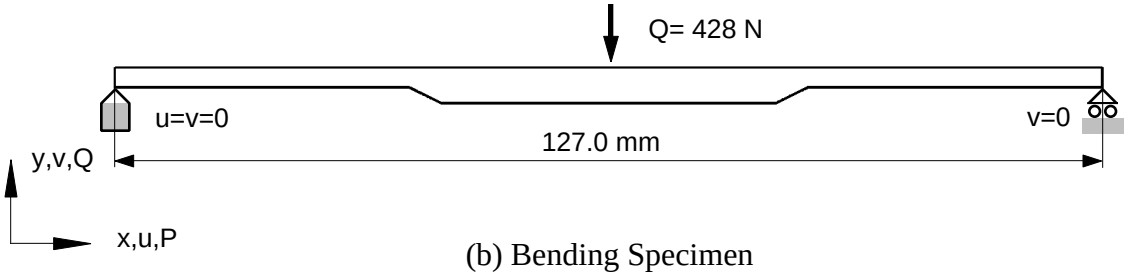

(b) Bending Specimen

Figure 16. Loads and Boundary Conditions For Tension and Three-Point Bending Case.

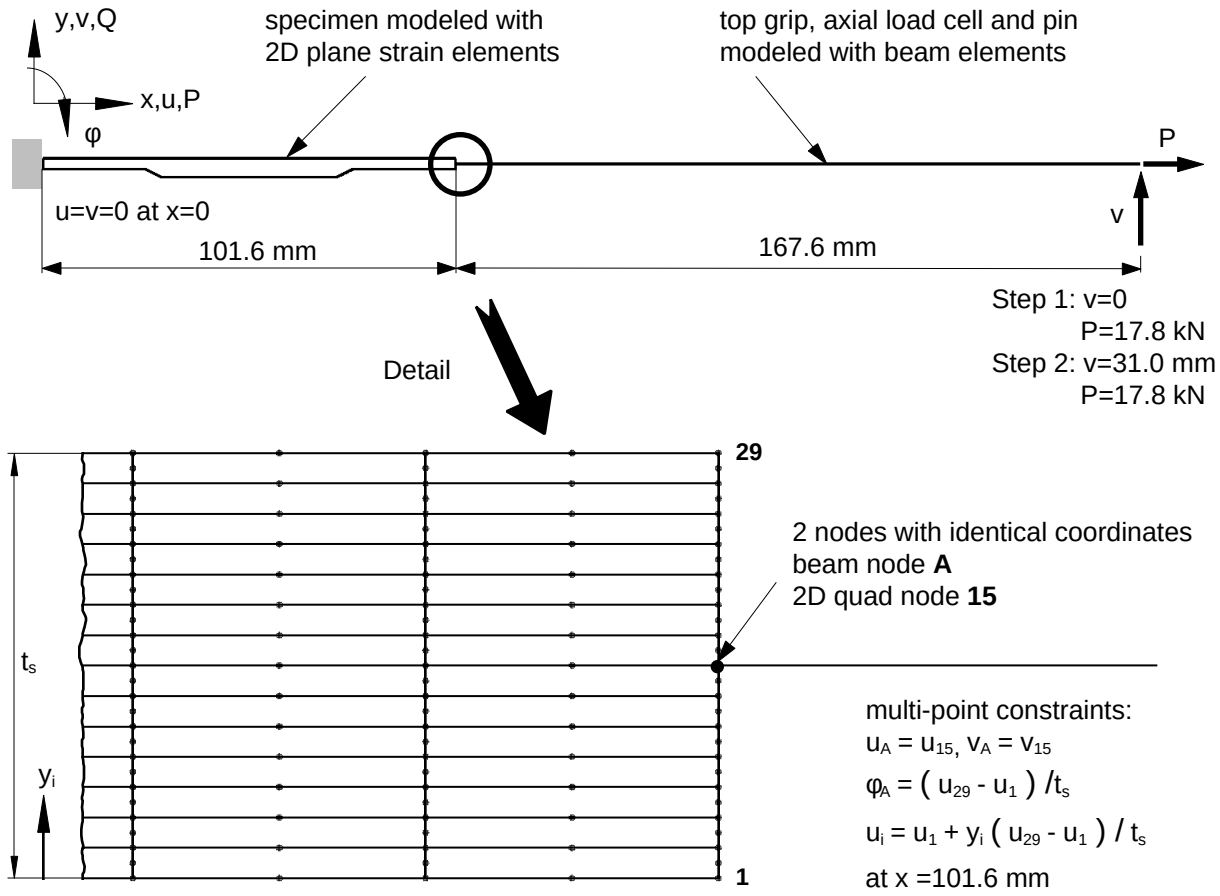

Figure 17. Loads and Boundary Conditions for the Combined Axial Tension and Bending Test.

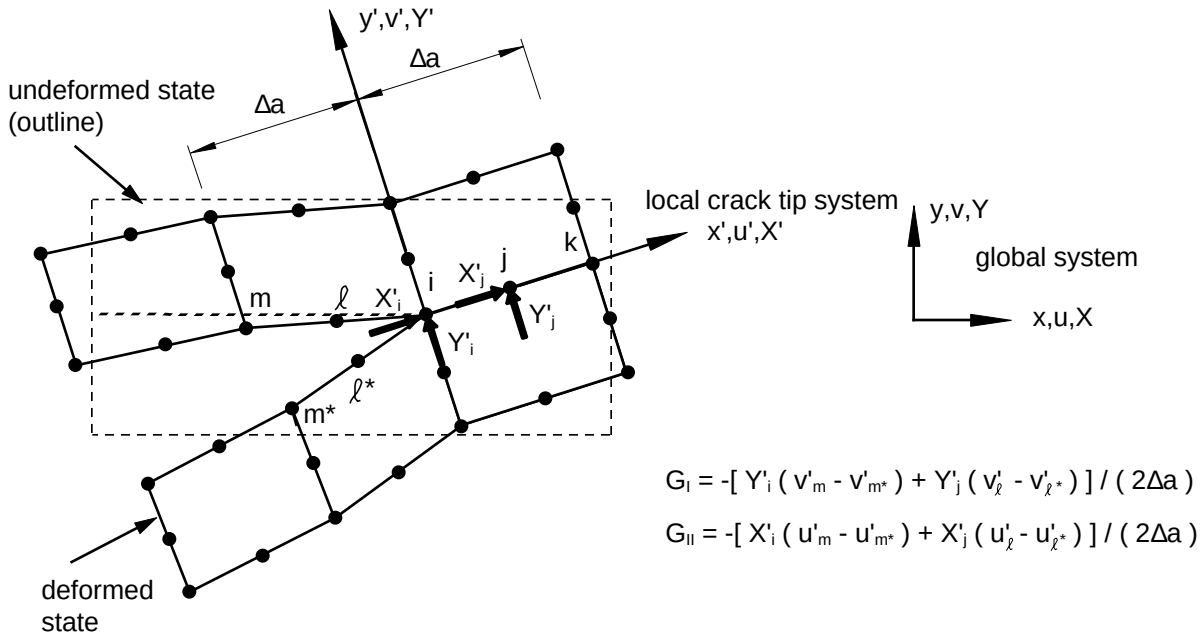

Figure 18. Virtual Crack Closure Technique (VCCT).

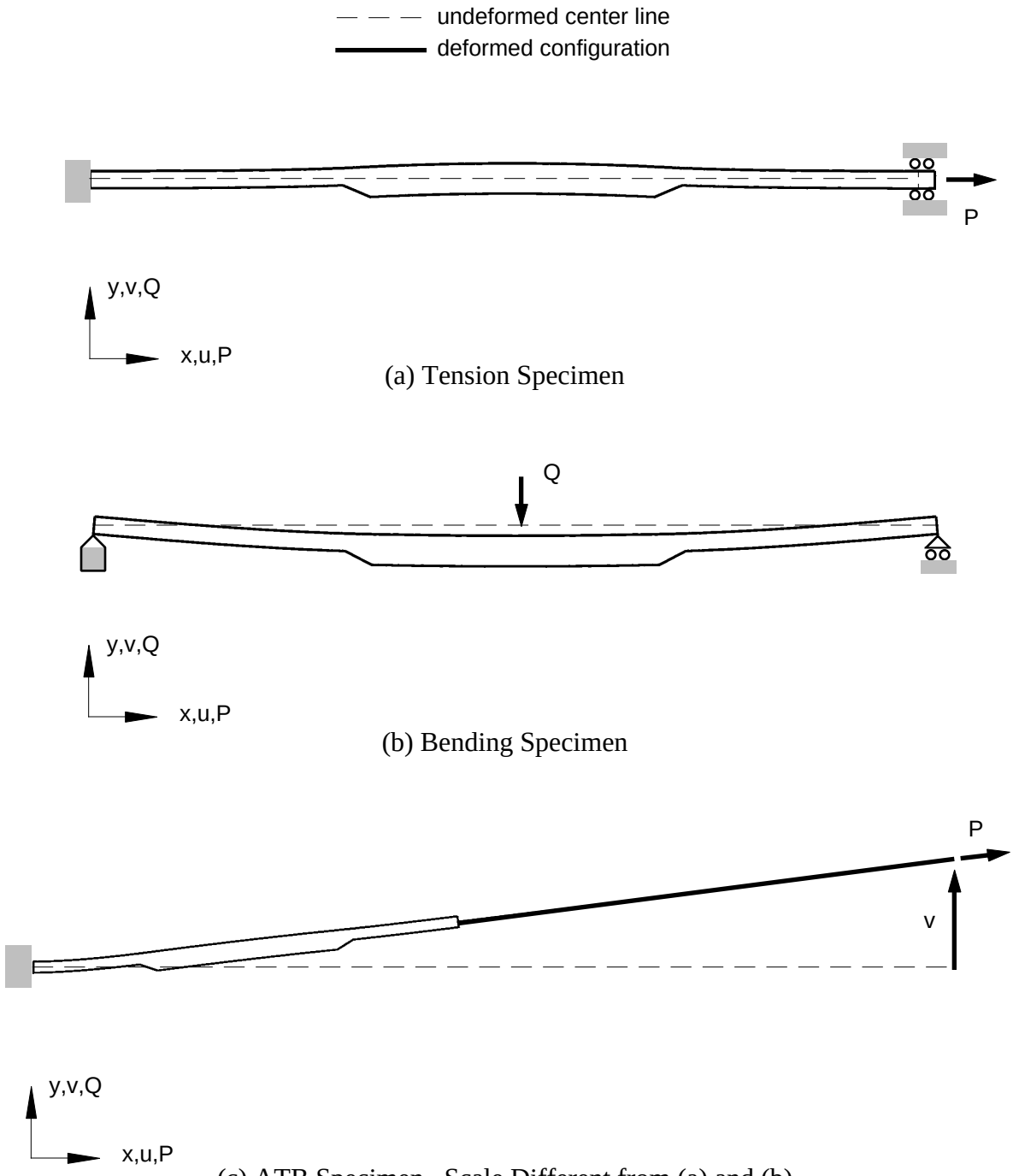

Figure 19. Deformed Test Specimen Geometries

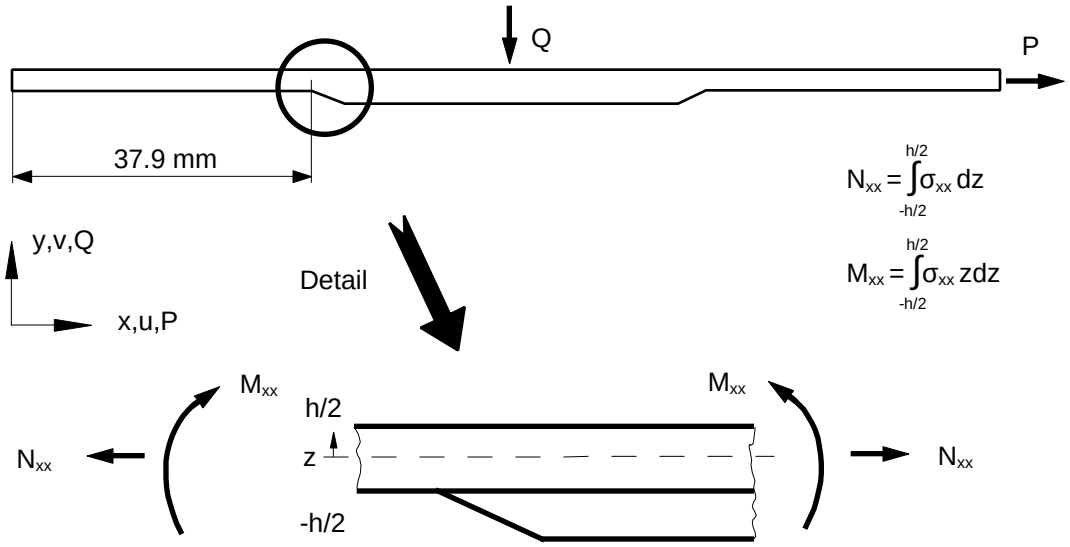

Figure 20. Calculation of Force and Moment Resultants.

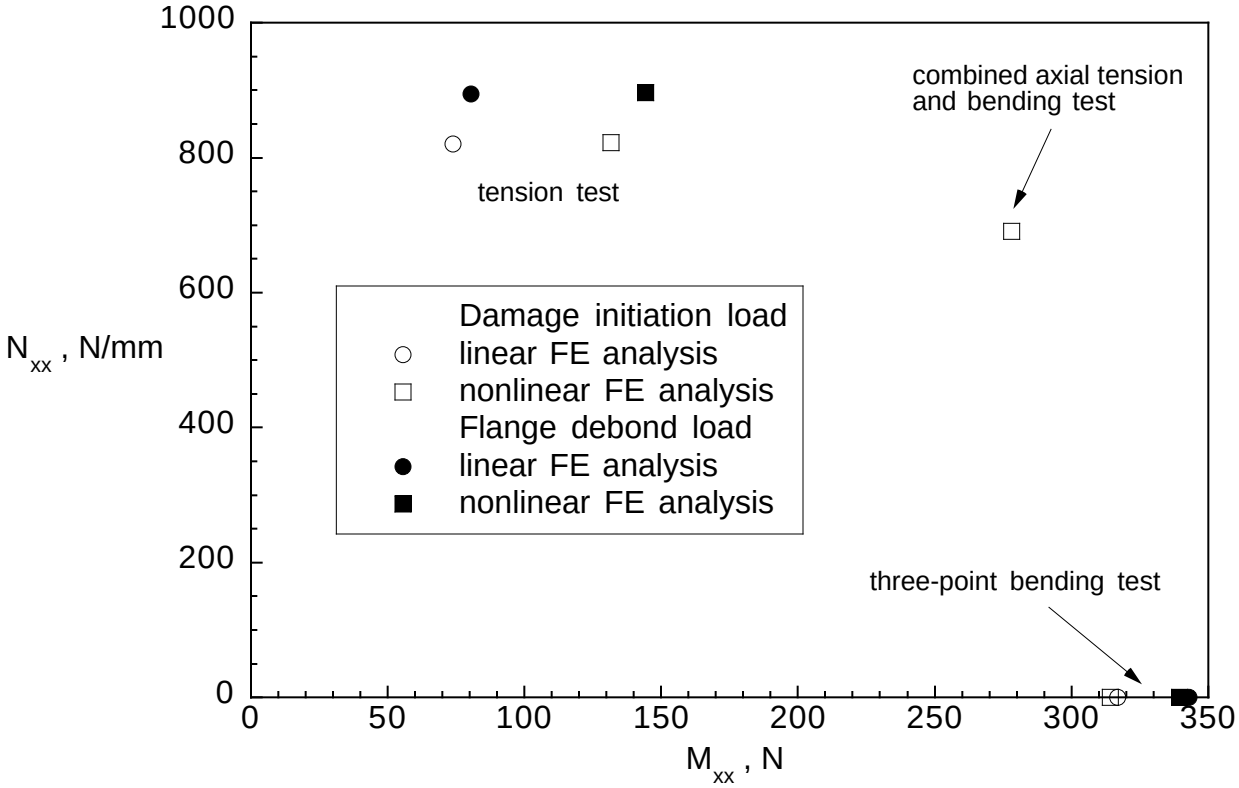

Figure 21. Computed Force and Moment Resultants at Flange Tip.

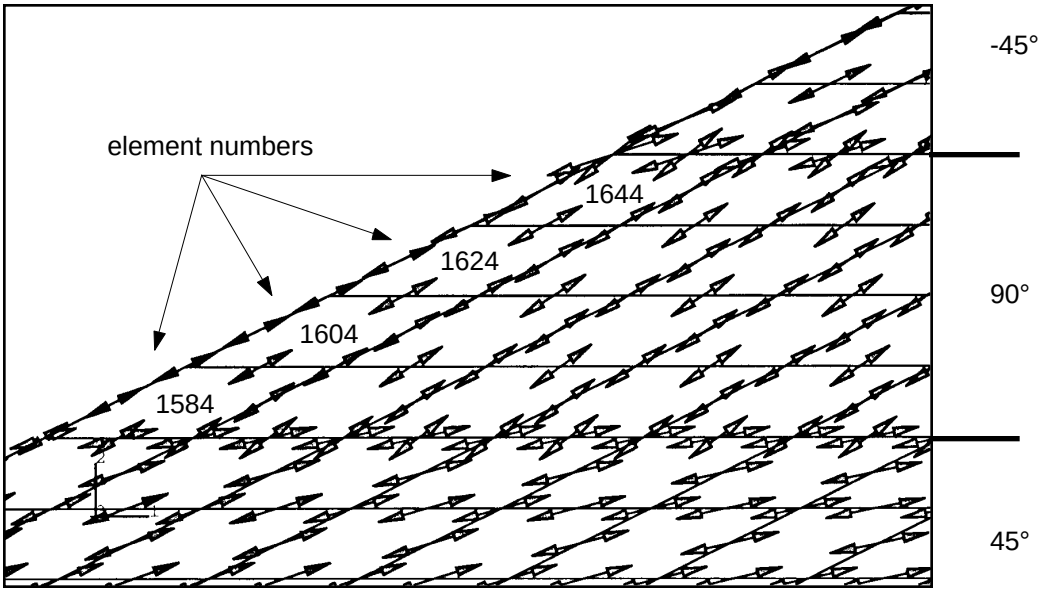

Figure 22. Trajectories of Maximum Principal Stresses.

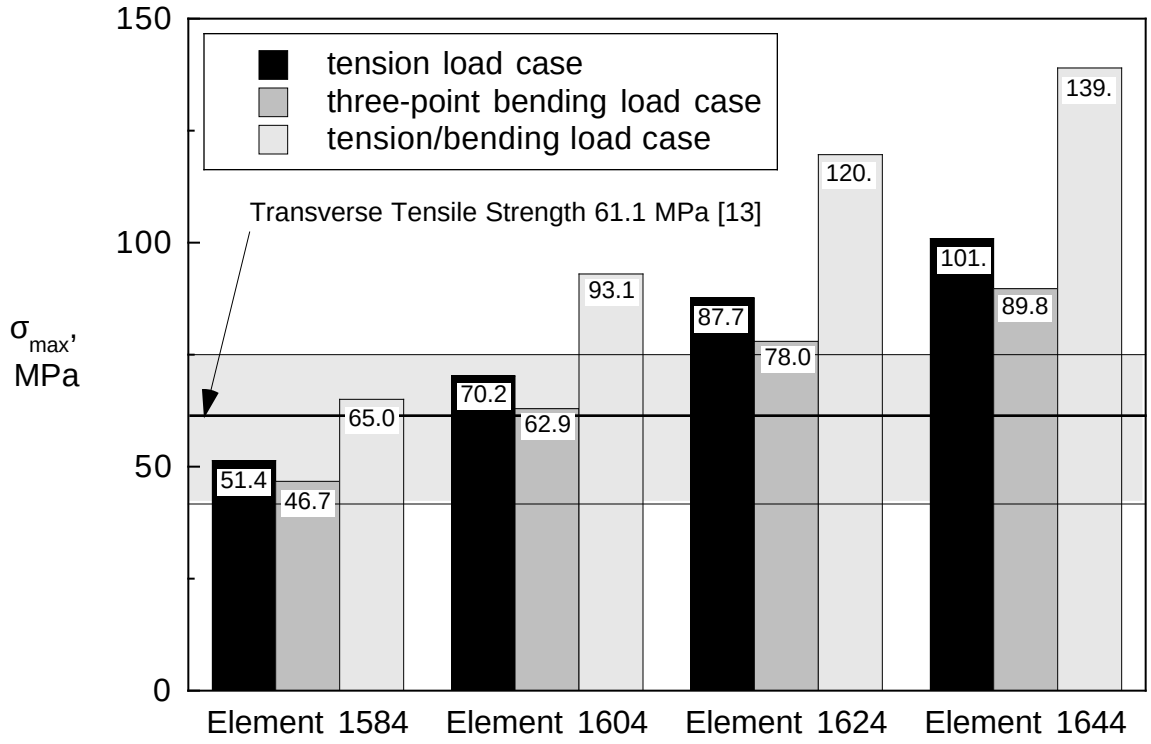

Figure 23. Comparison of Principal Tensile Stresses
Computed at Damage Initiation Load.

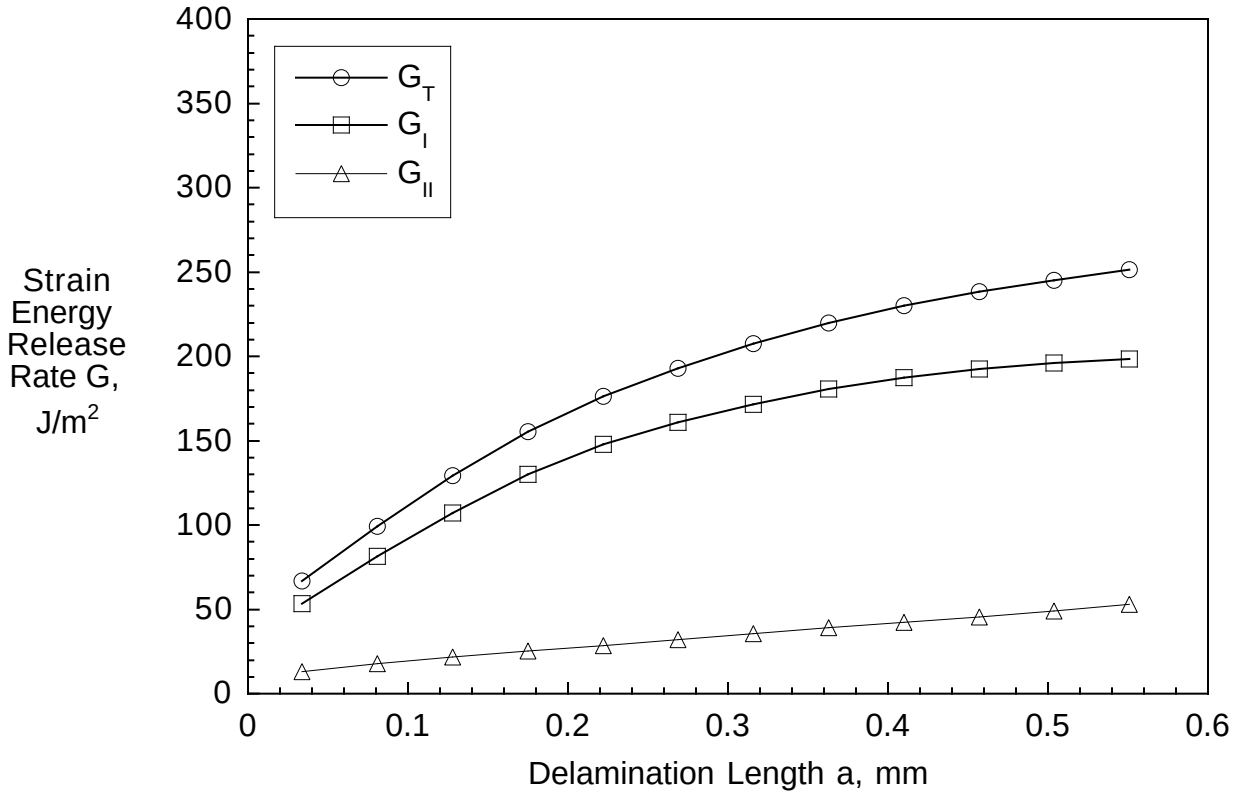

Figure 24. Computed Strain Energy Release Rates for Delamination Growth in a 90°/45° Flange Ply Interface for Tension Tests.

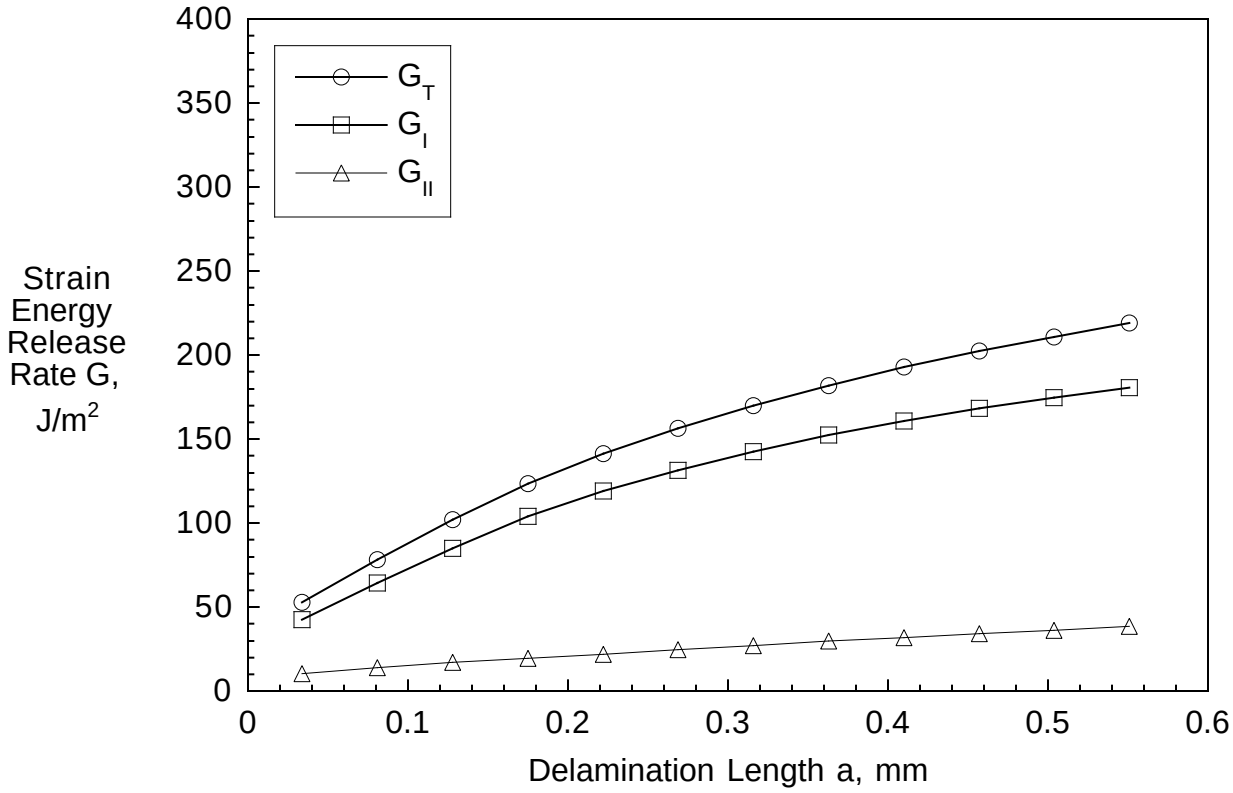

Figure 25. Computed Strain Energy Release Rates for Delamination Growth in a 90°/45° Flange Ply Interface for Three-Point Bending Tests.

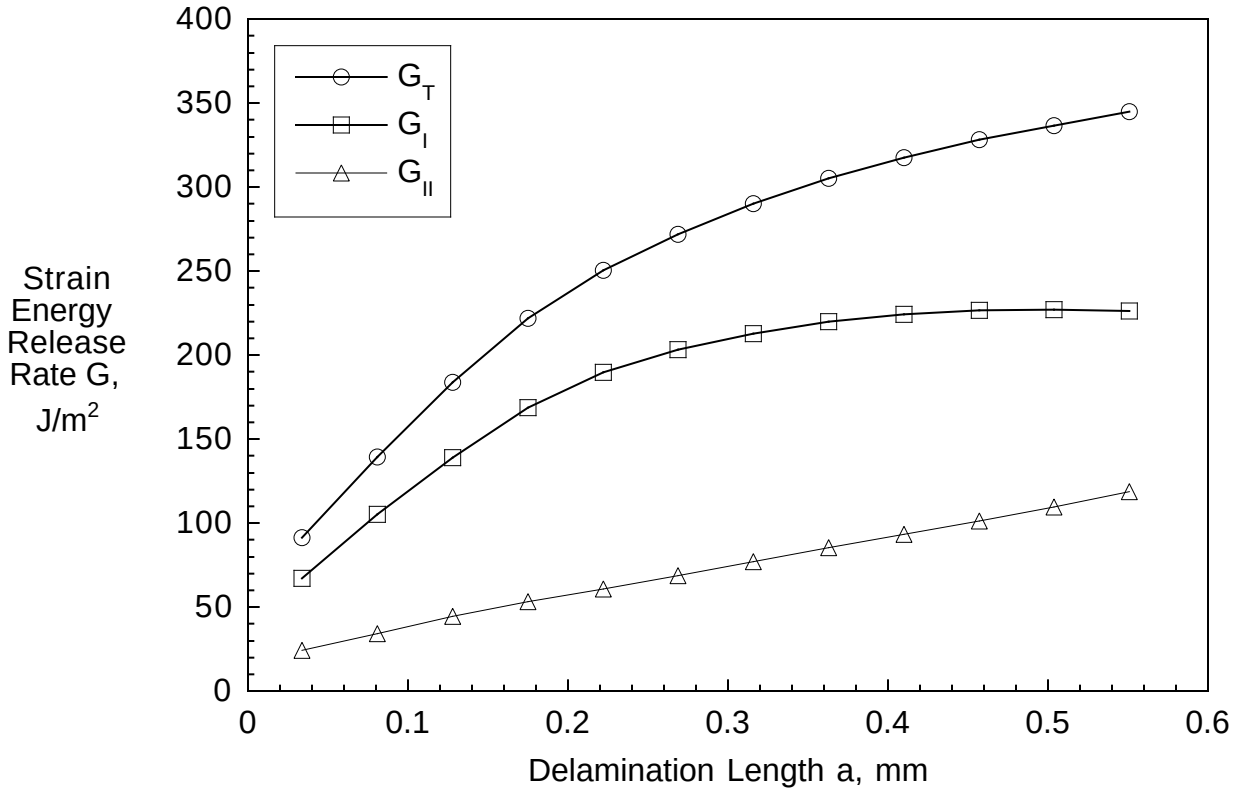

Figure 26. Computed Strain Energy Release Rates for Delamination Growth in a 90°/45° Flange Ply Interface for ATB Tests.

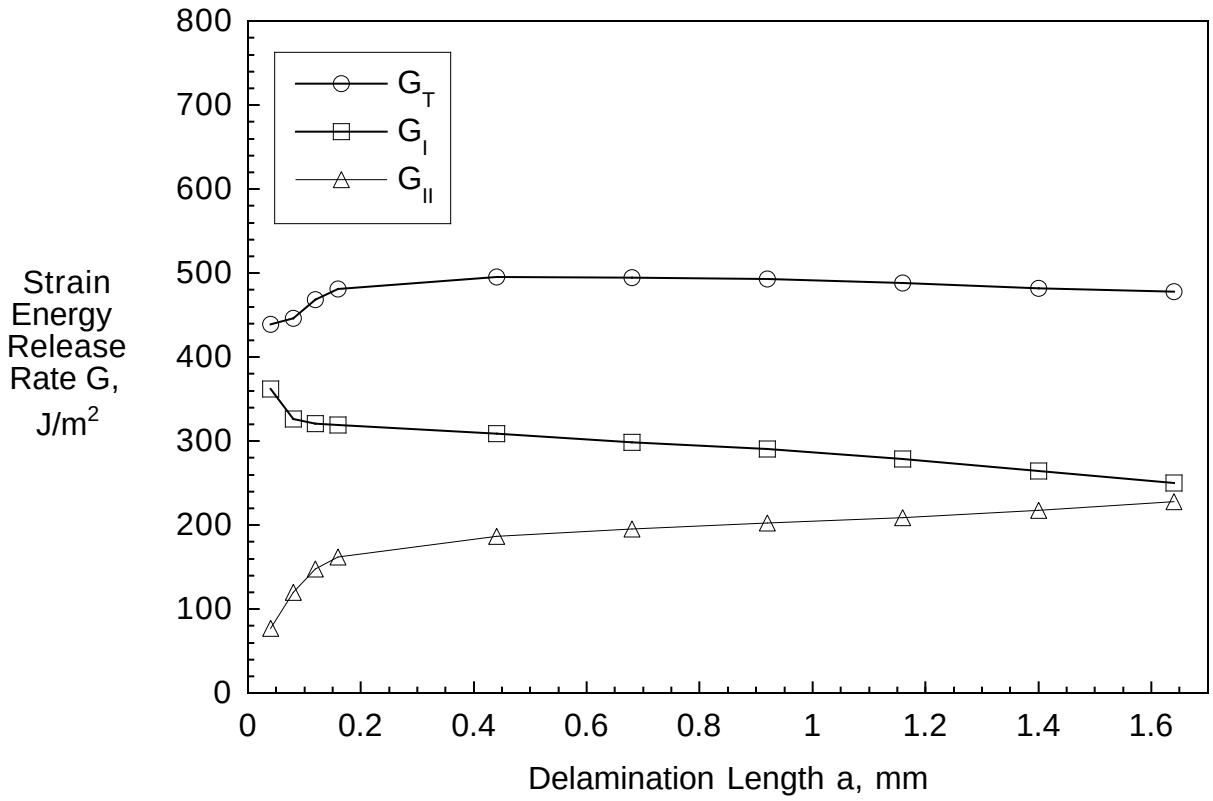

Figure 27. Computed Strain Energy Release Rates for Delamination Growth Between Adhesive and 0° Skin Ply for Tension Tests.

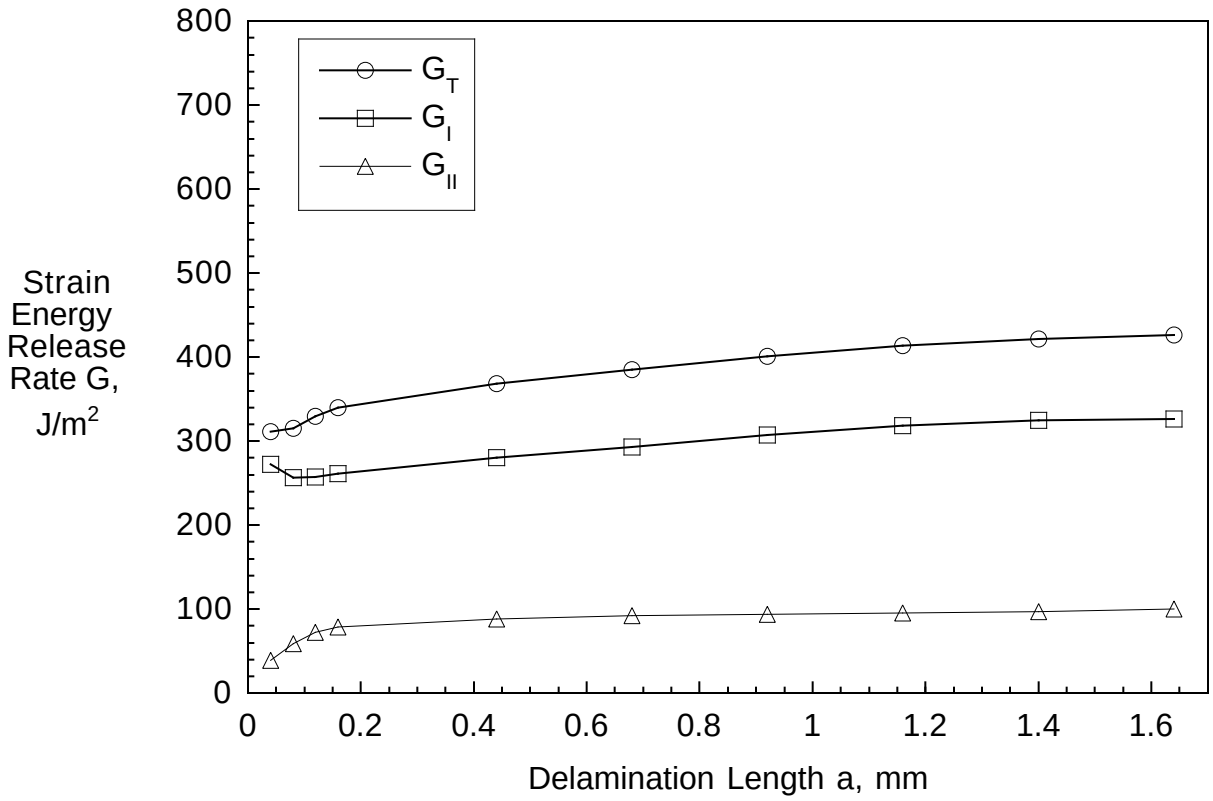

Figure 28. Computed Strain Energy Release Rates for Delamination Growth Between Adhesive and 0° Skin Ply for Three-Point Bending Tests.

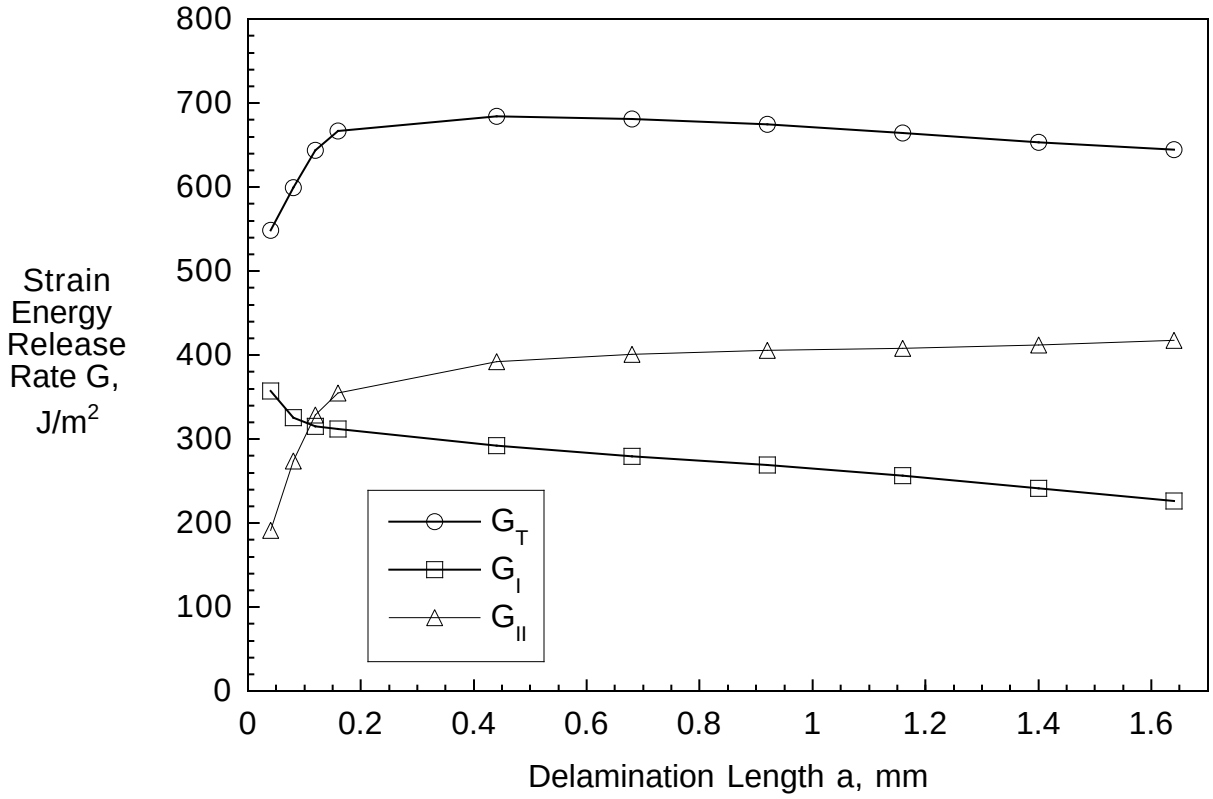

Figure 29. Computed Strain Energy Release Rates for Delamination Growth Between Adhesive and 0° Skin Ply for ATB Tests.

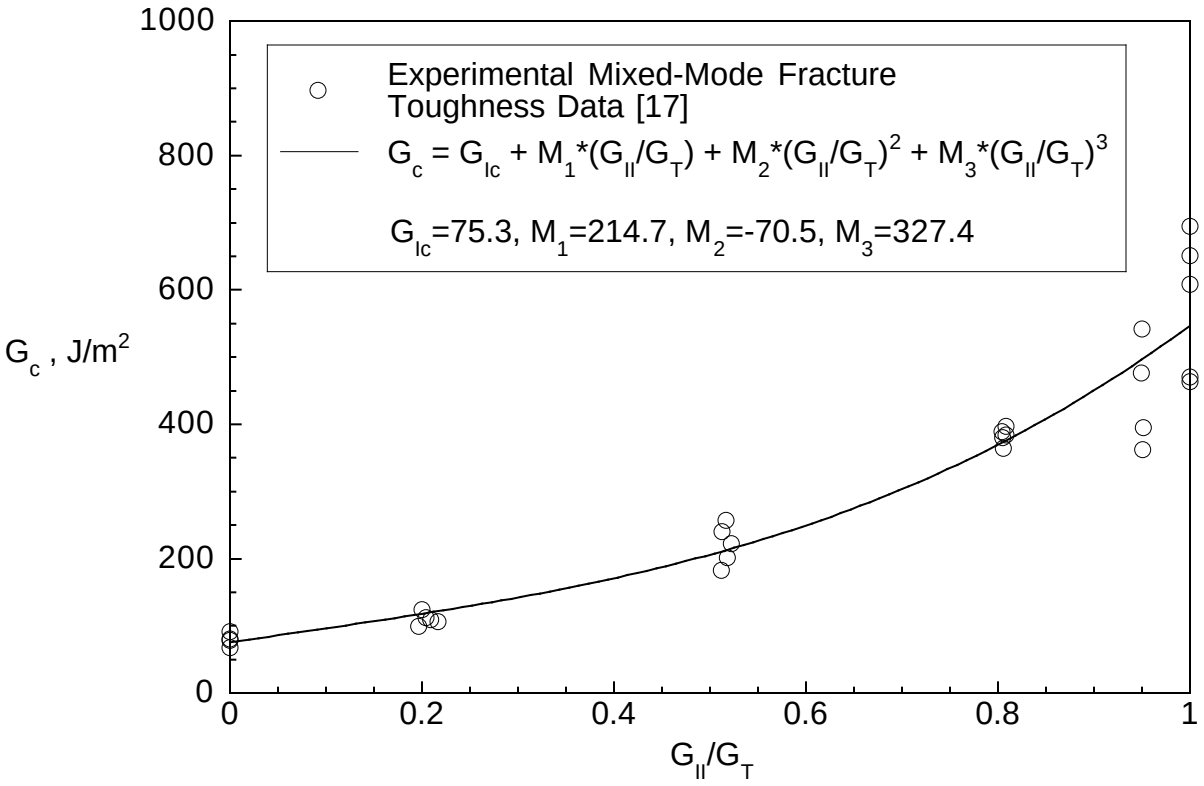

Figure 30. Mixed-Mode Delamination Criterion for AS4/3501-6 [18].

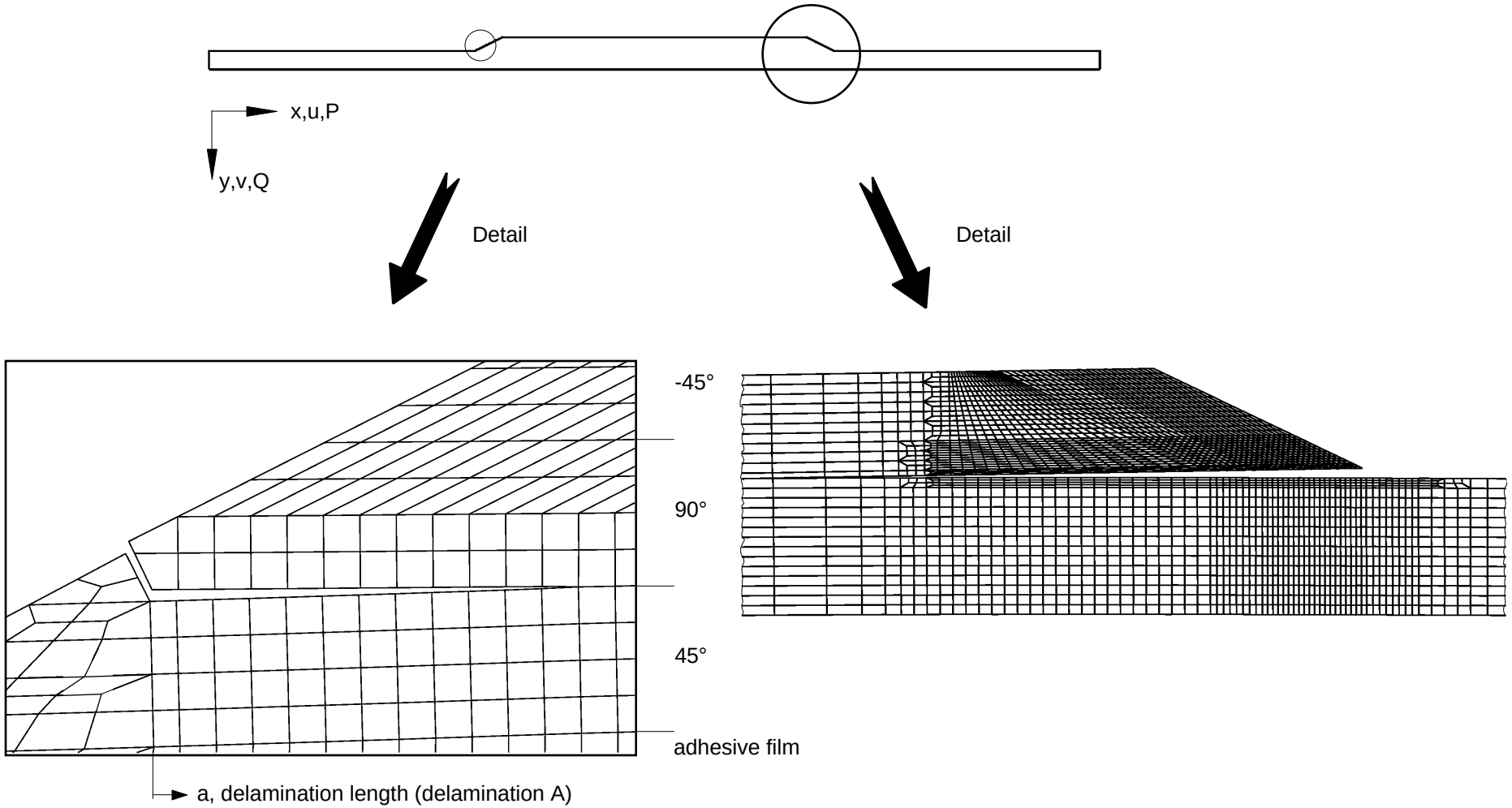

Figure 31. Finite Element Model of a Damaged Specimen.

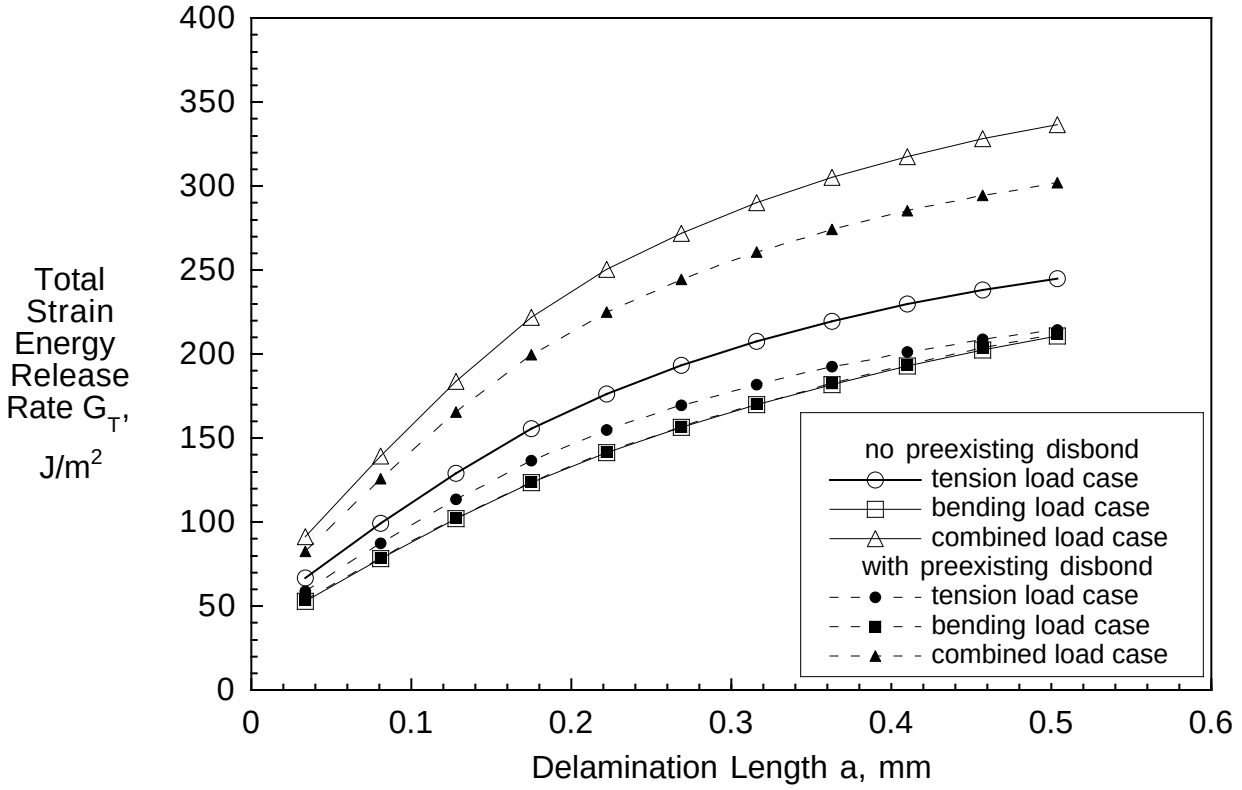

Figure 32. Computed Strain Energy Release Rates for Delamination Growth in a 90°/45° Flange Ply Interface with and without a Preexisting Disbond Between Adhesive and 0° Skin Ply.

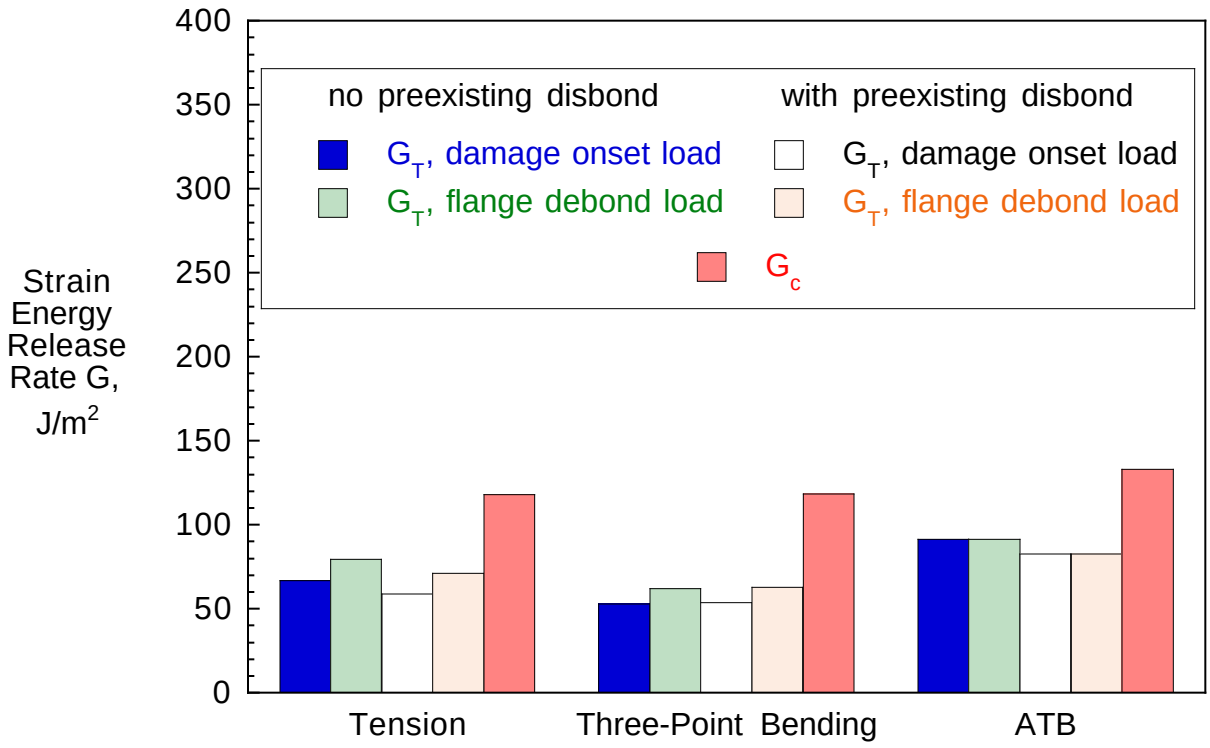

Figure 33. Comparison of Computed Total Strain Energy Release Rates in a 90°/45° Flange Ply Interface with Mixed-Mode Fracture Toughnesses.